Monthly Notices of the ROYAL ASTRONOMICAL SOCIETY
MNRAS **450,** 2373–2392 (2015) doi:10.1093/mnras/stv759

# SN 2013ab: a normal Type IIP supernova in NGC 5669

Subhash Bose,[1,2★] Stefano Valenti,[3,4] Kuntal Misra,[1] Maria Letizia Pumo,[5,6,7] Luca Zampieri,[5] David Sand,[8] Brijesh Kumar,[1] Andrea Pastorello,[5] Firoza Sutaria,[9] Thomas J. Maccarone,[8] Brajesh Kumar,[1,10] M. L. Graham,[11] D. Andrew Howell,[3,4] Paolo Ochner,[5] H. C. Chandola[2] and Shashi B. Pandey[1]

[1]*Aryabhatta Research Institute of Observational Sciences, Manora Peak, Nainital 263002, India*
[2]*Centre of Advance Study, Department of Physics, Kumaun University, Nainital 263001, India*
[3]*Las Cumbres Observatory Global Telescope Network, 6740 Cortona Dr., Suite 102, Goleta, CA 93117, USA*
[4]*Department of Physics, University of California, Santa Barbara, Broida Hall, Mail Code 9530, Santa Barbara, CA 93106-9530, USA*
[5]*INAF, Osservatorio Astronomico di Padova, I-35122 Padova, Italy*
[6]*Università di Catania, Dip. di Fisica e Astronomia (Sez. astrofisica), via S. Sofia 78, I-95123 Catania, Italy*
[7]*INAF-Osservatorio Astronomico di Palermo, Piazza del Parlamento 1, I-90134 Palermo, Italy*
[8]*Physics Department, Texas Tech University, Lubbock, TX 79409, USA*
[9]*Indian Institute of Astrophysics, Block-II, Koramangala, Bangalore 560034, India*
[10]*Institut d'Astrophysique et de Géophysique, Université de Liège, Allée du 6 Août 17, Bât B5c, B-4000 Liège, Belgium*
[11]*Department of Astronomy, University of California, Berkeley, CA 94720-3411 USA*

Accepted 2015 April 2. Received 2015 March 22; in original form 2015 January 13

## ABSTRACT

We present densely sampled ultraviolet/optical photometric and low-resolution optical spectroscopic observations of the Type IIP supernova 2013ab in the nearby (∼24 Mpc) galaxy NGC 5669, from 2 to 190 d after explosion. Continuous photometric observations, with the cadence of typically a day to one week, were acquired with the 1–2 m class telescopes in the Las Cumbres Observatory Global Telescope network, ARIES telescopes in India and various other telescopes around the globe. The light curve and spectra suggest that the supernova (SN) is a normal Type IIP event with a plateau duration of ∼80 d with mid-plateau absolute visual magnitude of −16.7, although with a steeper decline during the plateau (0.92 mag 100 $d^{-1}$ in *V* band) relative to other archetypal SNe of similar brightness. The velocity profile of SN 2013ab shows striking resemblance with those of SNe 1999em and 2012aw. Following the Rabinak & Waxman prescription, the initial temperature evolution of the SN emission allows us to estimate the progenitor radius to be ∼800 $R_\odot$, indicating that the SN originated from a red supergiant star. The distance to the SN host galaxy is estimated to be 24.3 Mpc from expanding photosphere method. From our observations, we estimate that 0.064 $M_\odot$ of $^{56}$Ni was synthesized in the explosion. General relativistic, radiation hydrodynamical modelling of the SN infers an explosion energy of 0.35 × $10^{51}$ erg, a progenitor mass (at the time of explosion) of ∼9 $M_\odot$ and an initial radius of ∼600 $R_\odot$.

**Key words:** supernovae: general – supernovae: individual: SN 2013ab – galaxies: individual: NGC 5669.

## 1 INTRODUCTION

Type IIP supernovae (SNe) are a sub-class of core-collapse SNe (CCSNe) whose progenitors had retained substantial amount of hydrogen before they exploded as SNe. These SNe exhibit nearly constant brightness in their light curve for a few months after explosion, known as plateau phase. This is explained as a combined effect of expanding ejecta and receding recombination layer of hydrogen due to adiabatic cooling of the envelope (e.g. Kasen & Woosley 2009). After reaching the end of plateau phase, a Type IIP SN light curve shows a very steep decline and then finally settles on to a relatively slowly declining phase labelled as the radioactive tail. This stage, also called the nebular phase, is powered by the radiation originating from the radioactive decay of $^{56}$Co to $^{56}$Fe (Arnett 1980) which in turn depends upon the amount $^{56}$Ni synthesized in the explosion.

Type IIP SNe are also proven candidates for distance estimation at extragalactic scales. Hamuy (2001) explored the potential of these

★ E-mail: email@subhashbose.com

SNe as standardizable candles. The expanding photosphere method (EPM; Kirshner & Kwan 1974) for estimating distances has also been applied extensively. Significant contribution has been made to improve and implement EPM by several authors, viz. Hamuy et al. (2001), Dessart & Hillier (2005c), Jones et al. (2009) and Bose & Kumar (2014). EPM requires an extensive set of photometric and spectroscopic data of SNe.

According to our current understanding of stellar evolution, Type IIP SNe originate from red supergiant (RSG) stars having initial masses of 9–25$M_\odot$, with an upper mass limit of ∼32 $M_\odot$, for solar metallicity stars (e.g. Heger et al. 2003). Recent studies also identified super-asymptotic giant branch stars as potential progenitors of some SNe IIP (see e.g. Pumo et al. 2009, and references therein). However, there is a limited number of nearby SNe where high-resolution pre-SN *Hubble Space Telescope* images are available. The estimated range of masses for these progenitors from direct observations lies within 9–17 $M_\odot$ (Smartt et al. 2009). On the other hand, hydrodynamical modelling of a handful of well-studied SN light curves suggests that their progenitor masses are within 15–25 $M_\odot$ (Utrobin & Chugai 2009; Bersten, Benvenuto & Hamuy 2011).

The cosmological importance of Type IIP SNe and the ambiguity in the present understanding of their evolution and physical mechanisms are key motivations to study individual events with a range of properties. One of the best observed recent Type IIP event is SN 2013ab.

SN 2013ab was discovered on 2013 February 17.5 UTC, by Blanchard et al. (2013) in the galaxy NGC 5669 (∼25 Mpc) (see Fig. 1) at $R \sim 17.6$ mag. The last non-detection was reported on February 15 (Zheng et al. 2013) to a limiting magnitude $R \sim 18.5$. We therefore adopt 2013 February 16.5(JD = 245 6340.0 ± 1.0 d) as the time of explosion (0 d phase) throughout the paper. Some basic parameters of SN 2013ab and its host galaxy are listed in Table 1.

In this work, we present results from optical photometric (*UBVRI* and *gri*) follow-up observations of SN 2013ab at 136 phases (from 3

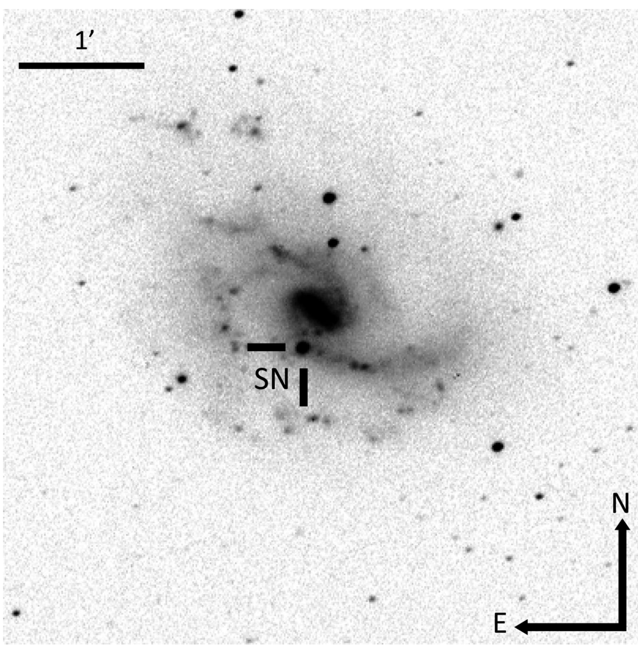


**Figure 1.** SN 2013ab in NGC 5669. The *V*-band image taken from 104-cm ST covering a sub-section of about 5.1 arcmin × 5.1 arcmin is shown.

**Table 1.** Properties of the SN 2013ab and its host galaxy NGC 5669.

| Parameters | Value | Ref.[a] |
|---|---|---|
| NGC 5669: | | |
| Type | Sb | 2 |
| RA (J2000) | $\alpha = 14^{\rm h}32^{\rm m}43\overset{\rm s}{.}8$ | 2 |
| DEC (J2000) | $\delta = 09°53'28\overset{''}{.}8$ | 2 |
| Abs. magnitude | $M_B = -19.28$ mag | 2 |
| Distance | $D = 24.0 \pm 0.9$ Mpc | 1 |
| Distance modulus | $\mu = 31.90 \pm 0.08$ mag | |
| Heliocentric velocity | $cz_{\rm helio} = 1374 \pm 2\,{\rm km\,s^{-1}}$ | 2 |
| SN 2013ab: | | |
| RA (J2000) | $\alpha = 14^{\rm h}32^{\rm m}44\overset{\rm s}{.}49$ | 3 |
| DEC (J2000) | $\delta = 09°53'12\overset{''}{.}3$ | |
| Galactocentric location | $7\overset{''}{.}5$ E, $18\overset{''}{.}1$ S | |
| Time of explosion | $t_0$ = 2013 February16.5 (UT) (JD 245 6340.0 ± 1.0) d | 1 |
| Total reddening | $E(B-V) = 0.044 \pm 0.066$ mag | 1 |

(1) This paper; (2) HyperLEDA – http://leda.univ-lyon1.fr (Makarov et al. 2014); (3) Zheng et al. (2013).

to 190 d), *Swift* Ultraviolet/Optical Telescope (UVOT) observations at 25 epochs (from 4 to 103 d) and low-resolution optical spectroscopic observations at 25 phases (from 2 to 184 d). The paper is organized as follows. Section 2 provides details of the photometric and spectroscopic observations. Determination of reddening and extinction is described in Section 3. In Section 4, we study the light and colour curves, derive bolometric light curves whose tail luminosities are used to estimate the $^{56}$Ni mass. In Section 5, we study the spectral evolution, present SYNOW modelling and derive line velocities. Application of EPM and estimate of distance to SN is described in Section 6. Hydrodynamical modelling to estimate physical parameters is described in Section 7. A brief summary of the work is given in Section 8.

## 2 OBSERVATIONS

Broad-band photometric data have been collected in Johnson *BV* and Sloan *gri* systems using the Las Cumbres Observatory Global Telescope (LCOGT) network, description of instrument and telescopes are presented in Brown et al. (2013). We have also used ARIES 104-cm Sampurnanand Telescope (ST) and the 130-cm Devasthal Fast Optical Telescope (DFOT) to acquire broad-band data in Johnson–Cousin *UBVRI* filters. The instrument details are presented in Bose et al. (2013) and Sagar et al. (2012). *Swift* UVOT has also observed SN 2013ab in ultraviolet (UV) and optical broadbands. A detailed description of data reduction and derivation of photometric magnitudes are given in Appendix A.

Low-resolution spectroscopic observations have been carried out at 25 phases from 2 to 184 d after explosion: 12 epochs of data were collected using Floyds spectrograph on Faulkes Telescope North (FTN), six epochs on Faulkes Telescope South (FTS), five epochs using HFOSC on Himalayan Chandra Telescope (HCT) and two epochs using the B&C spectrograph mounted on Galileo Telescope in Asiago. The data reduction process is given in Appendix B and the journal of spectroscopic observations in Table B1.

## 3 EXTINCTION AND DISTANCE

In order to derive intrinsic properties of the explosion, the line-of-sight reddening of SN 2013ab due to interstellar dust in both the Milky Way and the host galaxy should be known accurately. Using all-sky dust-extinction map of Schlafly & Finkbeiner (2011),[1] we adopt the following value of Galactic reddening: $E(B-V)_{\rm MW} = 0.0234 \pm 0.0002$ mag.

One of the widely adopted techniques for reddening estimate is using the narrow Na I D interstellar absorption dips. The equivalent width of Na I D absorption feature is found to be correlated with the reddening $E(B-V)$ estimated from the tail of SN Ia colour curves (Barbon et al. 1990; Turatto, Benetti & Cappellaro 2003). However, in our low-resolution set of spectra, we did not identify any Na I D absorption feature indicating that extinction due to the host galaxy is very low and of the order of Galactic reddening. To further constrain $E(B-V)$ due to the host galaxy, we implement 'colour-method' (Olivares et al. 2010), which assumes that at the end of plateau phase the intrinsic $(V-I)$ colour is constant. Thus, it is possible to obtain the host colour excess from observed $(V-I)$ colour and relate it to the visual extinction. The relation found by Olivares et al. (2010) is

$$A_V(V-I) = 2.518[(V-I) - 0.656] \quad (1)$$

$$\sigma_{(A_V)} = 2.518\sqrt{\sigma^2_{(V-I)} + 0.053^2 + 0.059^2}. \quad (2)$$

Using the mean $(V-I)$ colour within 78–82 d (corresponds to the end of plateau phase), and correcting it for Galactic reddening, we obtain $A_{V_{\rm host}} = 0.0624 \pm 0.2060$ mag which corresponds to $E(B-V)_{\rm host} = 0.0201 \pm 0.0664$ mag assuming total-to-selective extinction $R_V = 3.1$. Hereafter, we adopt a total $E(B-V) = 0.044 \pm 0.066$ mag along the line of sight to SN 2013ab providing a total $A_V = 0.14 \pm 0.21$ mag.

To seek further justification of the derived $E(B-V)$, we look into the earliest spectra at 2.2 d. At early phases, the spectral energy distribution (SED) can be well approximated as a blackbody. Hence, we de-redden the spectra with different values of $E(B-V)$ and estimate corresponding blackbody temperatures (see Fig. 2). For $E(B-V) = 0.30$ mag, we obtain an unphysically high temperature of 170 kK. The theoretical modelling of Dessart & Hillier (2006) and Bersten et al. (2011) indicate that for a 2.2 d old Type IIP SN, the temperature must be around 25–30 kK. Our blackbody fit to the spectra with $E(B-V) = 0.10$ mag results in a temperature estimate of 22.3 kK. This is consistent with the values predicted by theoretical modelling. Also, we estimate a temperature of 18.7 kK corresponding to our adopted $E(B-V) = 0.044$ mag. This analysis provides an approximate upper limit of $E(B-V) = 0.10$ mag which is consistent with the adopted reddening value determined using the colour-method.

A number of distance estimates to NGC 5669 using the Tully–Fisher method are available in the literature with a wide variation in values ranging from 18 to 32 Mpc. Hence to seek for a reliable estimate, we applied EPM to the SN and derived a distance of 24.26 ± 0.98 Mpc. The detailed EPM analysis will be discussed in Section 6. We adopt the distance to host galaxy to be 24.0 ± 0.9 Mpc which is the weighted mean of EPM and two other recent Tully–Fisher estimates from the literature, viz. Theureau et al. (2007, 25.23 ± 4.65 Mpc) and Tully et al. (2009, 19.67 ± 3.35 Mpc), assuming $H_0 = 73$ km s$^{-1}$Mpc$^{-1}$, $\Omega_{\rm m} = 0.27$, $\Omega_\Lambda = 0.73$.

[1] http://irsa.ipac.caltech.edu/applications/DUST/

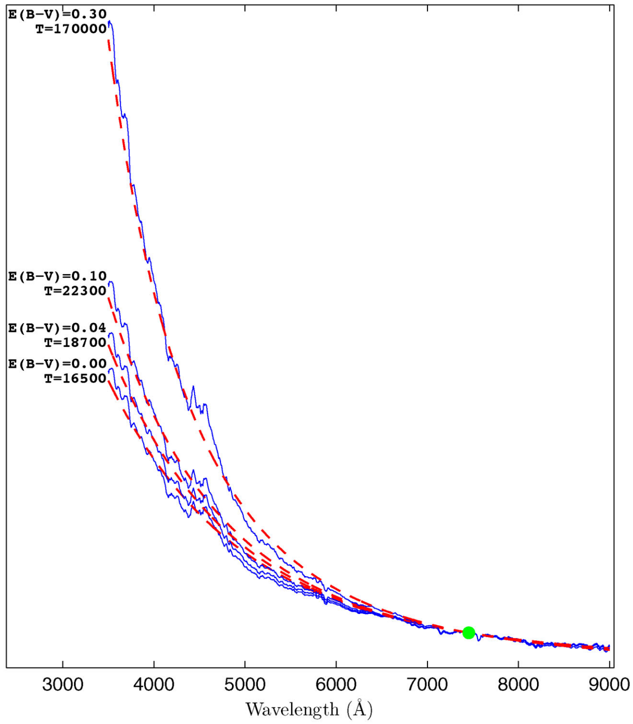


**Figure 2.** The SED of SN 2013ab at 2.2 d is compared with a blackbody function (dotted line). The fluxes are normalized relative to an arbitrary line-free region in the spectra marked with a green filled circle. Temperature units are kelvin (K) and $E(B-V)$ in magnitude.

## 4 OPTICAL LIGHT CURVE

### 4.1 Apparent magnitude light curves

Photometric measurements in Johnson–Cousins *UBVRI* and SDSS *gri* are available at 136 phases from 1 to 189 d after the explosion, with a stringent non-detection at −1 d. Additional 25 epoch observations are from *Swift* UVOT in all six UVOT filters. The resulting light curves are shown in Fig. 3 and data are tabulated in Table A1.

The early light curve initially shows a sharp rise in *r* band, which is also visible in all other optical bands as well, but only during first few phases. Then, the light curve declines slowly until the end of plateau-phase. Since 95 d, a steep decline to the radioactive nebular tail follows. After that, since ∼113 d, the light curve settles on to this relatively slower declining phase. Observations in the UVOT bands do not show any initial rise in the light curve, although observations started with the same delay as the optical bands (+4 d). The early peak is found to occur at 6.4, 7.2, 7.8, 8.3, 8.3, 7.8, 8.4 and 7.8 d in *UBVRIgri* bands respectively, with uncertainties of about 1 d. This is consistent with most fast-rising SNe (e.g SN 2005cs; Pastorello et al. 2009), and is significantly different from some SNe which exhibit a slow-rising early-phase light curve [see e.g. the delayed *V*-band maximum attained at 16 d in SN 2006bp (Quimby et al. 2007), 13d in SN 2009bw (Inserra et al. 2012a) and 15d in SN 2012aw (Bose et al. 2013)].

The decline rates after the initial maximum to the plateau-end in *UBVRIgri* are 7.60, 2.72, 0.92, 0.59, 0.30, 1.68, 0.77, 0.51 mag 100 d$^{-1}$, respectively. This is steeper than the values reported for SN 1999em (Leonard et al. 2002a), SN 1999gi (Leonard et al. 2002b) and SN 2012aw (Bose et al. 2013). For example in the *UBV* bands, SN 2012aw experienced a decline rate of 5.60, 1.74,

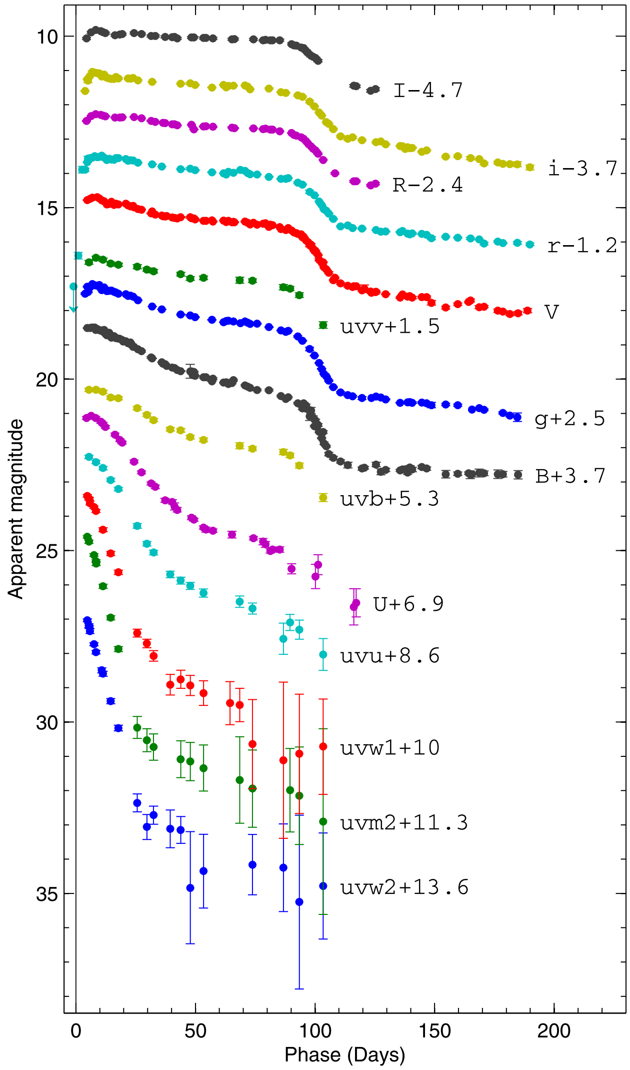


**Figure 3.** The photometric light curve of SN 2013ab in Johnson–Cousins *UBVRI*, SDSS *gri* and *Swift* UVOT bands. The light curves are shifted arbitrarily for clarity. The large errors in late UV data points are due to faint SN flux extracted after subtracting host background.

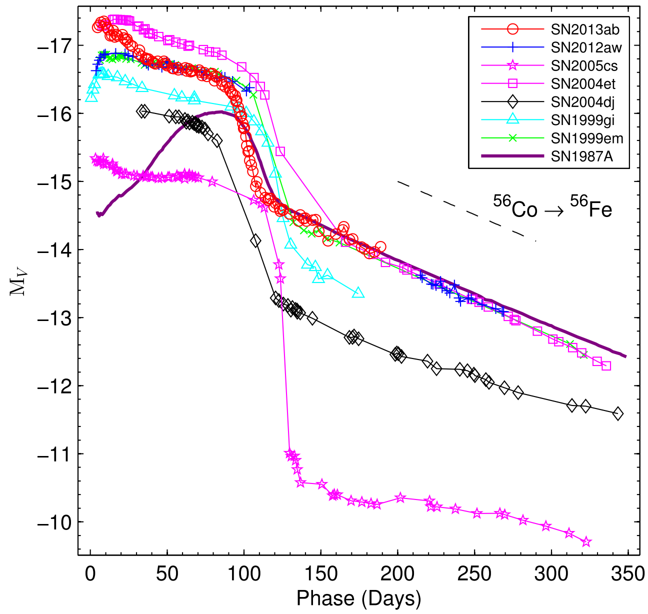


**Figure 4.** Comparison of the *V*-band absolute light curve of SN 2013ab with those of other Type IIP SNe. The exponential decline of the radioactive decay law is indicated with a dashed line. The time of explosion in JD-240 0000, distance in Mpc, reddening $E(B-V)$ in mag and the reference for apparent *V*-band magnitude, respectively, are : SN 1999em – 51475.6, 11.7, 0.10, Leonard et al. (2002a), Elmhamdi et al. (2003a); SN 2004et – 53270.5, 5.4, 0.41, Sahu et al. (2006); SN 2005cs – 53549.0, 7.8, 0.11, Pastorello et al. (2009); SN 2004dj – 53187.0, 3.5, 0.07, Tsvetkov, Goranskij & Pavlyuk (2008); SN 1987A – 46849.8, 0.05, 0.16, Hamuy & Suntzeff (1990); SN 1999gi – 51522.3, 13.0, 0.21, Leonard et al. (2002b); SN 2012aw – 56002.6, 9.9, 0.07, Bose et al. (2013).

0.55 mag 100 $\mathrm{d}^{-1}$. However, the decline rate of SN 2013ab is similar to that of SN 2004et (2.2 mag 100 $\mathrm{d}^{-1}$ in *B* band; Sahu et al. 2006). During the nebular phase, the decline rate (mag 100 $\mathrm{d}^{-1}$) of the light curves are estimated to be 0.36, 0.97, 0.76, 0.66 and 1.16 for *BVgri*, respectively.

SN 2013ab is luminous in the UVOT *UV* bands at early phases, but it declines steeply at a rate of 0.169, 0.236 and 0.257 mag $\mathrm{d}^{-1}$ in *uvw1, uvw2 and uvm2* bands, respectively. After 30 d, the light curves settle on a slow-declining plateau until ∼103 d corresponding also with the end of *Swift* UVOT observations. SN 2012aw is the only known SN which shows a UV plateau (Bayless et al. 2013) similar to that observed in SN 2013ab. Although, a UV plateau is expected, not many Type II SNe have been observed so far at these wavelengths until relatively late phases. This is possibly because of their low apparent brightness due to large distance and extinction, making them unsuitable for UVOT detections. However, these limitations did not hinder SN 2013ab making this event as one of the best-observed SNe IIP in the UV domain.

### 4.2 Absolute magnitude and colour evolution

The *V*-band absolute light curve of SN 2013ab is shown in Fig. 4, and is compared with those of other well-studied Type IIP SNe. All data are corrected for their corresponding distances and extinction values. SN 2013ab is compared with the normal SNe 1999em, 1999gi, 2004dj, 2004et and 2012aw; the sub-luminous SN 2005cs and the photometrically peculiar SN 1987A. The comparison shows that the *V*-band mid-to-late plateau absolute magnitude of SN 2013ab is very similar to those of SNe 1999em and 2012aw. However, the plateau light-curve decay rate, especially during the early-plateau (from 10 to 50 d) phase is significantly larger than those of SNe 1999em and 2012aw (by 1.58 and 2.61 times, respectively), although later on (during late-plateau phase) the slopes are somewhat similar. The decay rate of the early-plateau light curve is as high as 1.58 mag 100 $\mathrm{d}^{-1}$, which is significantly higher than that of the late-plateau light curve (0.49 mag 100 $\mathrm{d}^{-1}$). The nebular-phase light curve evolution follows a decay rate of 0.97 mag 100 $\mathrm{d}^{-1}$ which is similar to those of other SNe in our comparison sample. This is consistent with the expected decay rate of the $^{56}$Co to $^{56}$Fe (0.98 mag 100 $\mathrm{d}^{-1}$). The mid-plateau absolute magnitude is $M_V^p = -16.7$ mag, categorizing SN 2013ab as a normal Type IIP event (Patat et al. 1994). This magnitude make SN 2013ab significantly brighter than sub-luminous class of events like SN 2005cs ($M_V^p \sim -15$ mag; Pastorello et al. 2009). Another noticeable difference with the compared SNe is the relatively shorter plateau duration, ∼78 d in SN 2013ab, in contrast to ∼90 d and 92 d for SNe 1999em and 1999gi, respectively. Anderson et al. (2014b) found an anticorrelation between the slope of early plateau and full-plateau duration for Type II SNe, which is

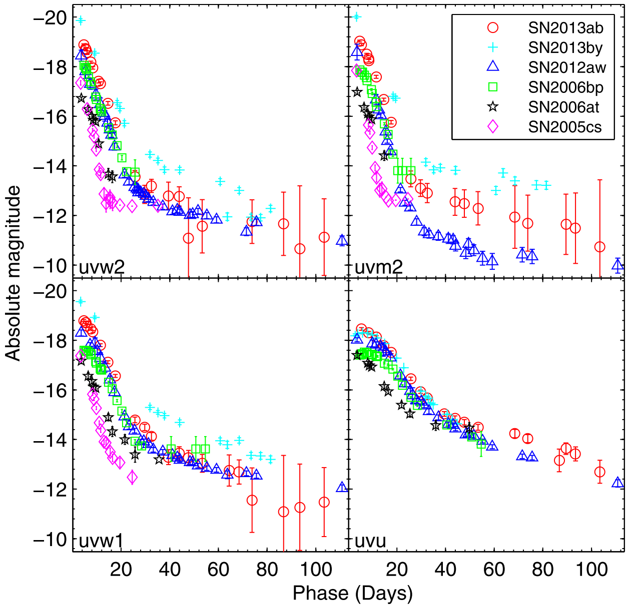


**Figure 5.** *Swift* UVOT UV absolute light curves of SN 2013ab, are compared with other well-observed IIP SNe from UVOT. For the compared SNe, references for UVOT data, extinction and distance are: SN 2005cs – Brown et al. (2009), Pastorello et al. (2009); SN 2006at – Brown et al. (2009), Distance 65 Mpc, $E(B-V) = 0.031$ mag (only Galactic reddening; Schlafly & Finkbeiner 2011); SN 2006bp – Dessart et al. (2008); SN 2012aw – Bayless et al. (2013), Bose et al. (2013); SN 2013by – Valenti et al. (2015).

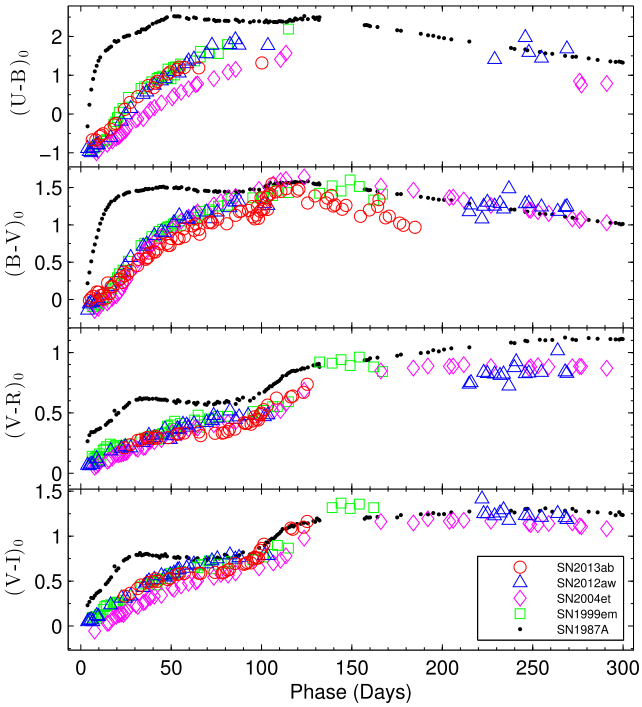


**Figure 6.** The evolution of intrinsic colours of SN 2013ab is compared with those of other well-studied Type IIP SNe 1987A, 1999em, 2004et and 2012aw. Reference for data are the same as in Fig. 4.

consistent with the faster decline but shorter plateau duration of SN 2013ab. However, it fits somewhat at the lower end of the scatter relation.

*Swift* UVOT absolute light curves (in *uvu, uvw1, uvm2* and *uvw2* bands) of SN 2013ab are shown in Fig. 5 and are compared with other well-observed IIP SNe. Distance and extinction has been corrected for each of the events. For SN 2006at, extinction is not known, hence a minimal reddening has been adopted accounting only for Milky Way extinction. SN 2013ab is on the brighter end among the compared events. Most SNe were not detected in UV after about a month, this is primarily due to large distances and extinction values. Both of these factors being not a major issue in SN 2013ab, which has been in fact observed for more than 100d. SNe 2012aw and 2013by are comparable with SN 2013ab in terms of data coverage and clear detection of a plateau in the UV domain. The plateau is evident in all UV bands after 30 d and follows a similar trend as that observed in SN 2012aw.

The broad-band colour evolution provides important information about the temporal variation of the SN envelope properties. The expansion and cooling behaviour of the envelope can be studied from the colour evolution at different phases. The intrinsic colour evolutions ($U-B, B-V, V-R$ and $V-I$) are shown in Fig. 6. All colours show a rapid evolution towards redder colours until ∼50 d, due to a rapid cooling of fast expanding ejecta. Thereafter, they evolve relatively slowly until the onset of the nebular phase. The colour evolution is very similar in other archetypal SNe IIP such as SN 1999em and SN 2012aw. The $(B-V)$ colour shows a bluer trend after 120 d, when the nebular phase begins. In this phase, the ejecta become sufficiently optically thin to allow photons from radioactive decay of $^{56}$Co to $^{56}$Fe to escape.

To have an idea of the temporal evolution of temperature and photospheric radius, we fit blackbody functions to the broad-band optical fluxes (after correcting for total line-of-sight extinction). The blackbody radii are further corrected by dilution factors (using the prescription of Dessart & Hillier 2005c) to estimate photospheric radii (where optical depth is $\tau = 2/3$) rather than thermalization radii. The plot with the photospheric temperature and radius evolutions is shown in Fig. 7. The temperature drops very rapidly from 5 to 25 d due to adiabatic cooling of the rapidly expanding envelope. Thereafter, the decline flattens as the SN progressively enters the nebular phase. The photospheric radius increases rapidly as the SN expands and thereafter the radius remains almost constant until

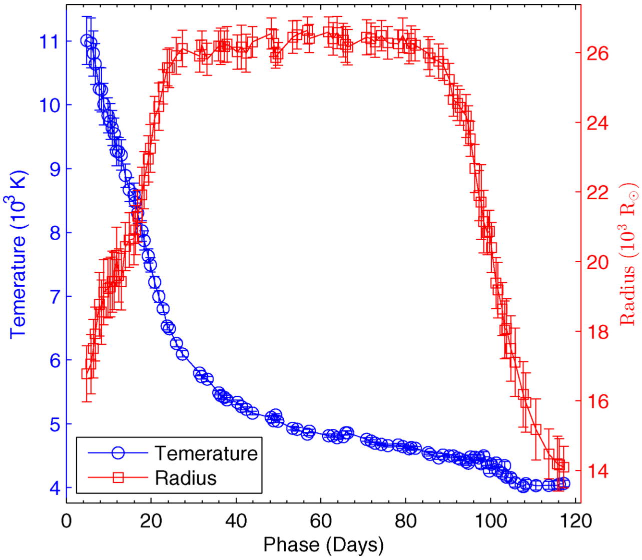


**Figure 7.** The evolutions of temperature and radius in SN 2013ab, as derived from blackbody fits to the observed fluxes in the optical range (0.36–0.81 μm).

around 85 d, which marks the end of plateau phase. This apparent contradiction to the expansion is due to the fact, that with the fall of temperature the ionized hydrogen starts to recombine by depleting the free electrons thereby optically thinning the outer ejecta. This results in a receding photospheric layer on top of the expanding envelope, ultimately leading to an unchanged photospheric radius. After 85 d, the radius falls off very rapidly with the end of the hydrogen recombination. During this phase, the ejecta become cooler and almost optically thin leaving behind no free electrons. Moreover, the dilution factor corrections are no longer applicable as radiation does not have thermal origin.

### 4.3 Bolometric light curve

Pseudo-bolometric luminosities have been computed at all phases adopting the same method as described in Bose et al. (2013), i.e. by constructing an SED from the extinction-corrected photometric fluxes which are semideconvolved from broad-band filter responses. At early phases ($\lesssim$30 d), when the SN is hot, the bolometric fluxes are dominated by the UV bands. At later phases ($\gtrsim$100 d), a major fraction of the bolometric contribution comes from infrared (IR) domain. The luminosity is computed within the optical domain (3335–8750 Å), which includes *UBVRI* and *gri* contributions. We have also used UVOT data in the bolometric luminosity computation which covers the wavelength range from the *uvw*2 to the *I* bands (1606–8750 Å). The contribution from the UV fluxes yields a significantly higher value of the early luminosity.

In Fig. 8, we plot the optical pseudo-bolometric luminosities of SN 2013ab along with other well-studied objects, including SNe 1987A, 1999em, 2004et, 2005cs, 2012aw. To have homogeneity in the comparison of bolometric light curves, all luminosities have been computed using the same algorithm and wavelength range. We also include UV–optical bolometric light curves of SNe 2013ab and 2012aw for comparison. The bolometric luminosity declines

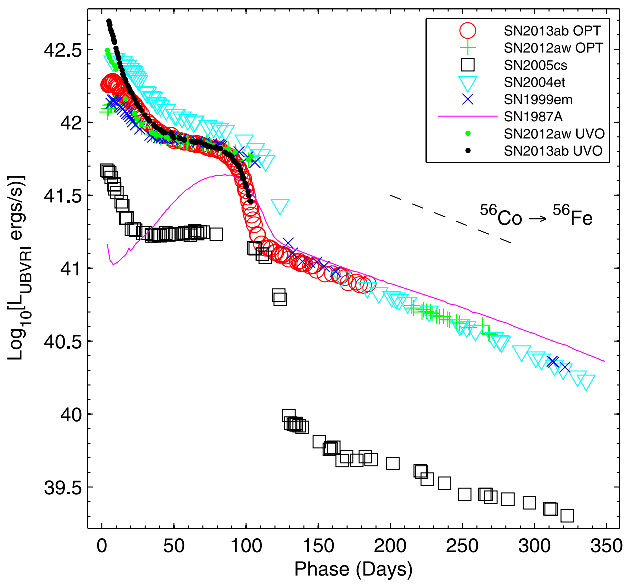


**Figure 8.** The *UBVRI* pseudo-bolometric light curve of SN 2013ab is compared with those of other well-studied SNe. Light curves with added UVOT UV contributions are also shown for SN 2013ab and SN 2012aw (labelled as UVO). The adopted distances, reddening and time of explosion values are same as in Fig. 4. The exponential decline of the radioactive $^{56}$Co decay law is shown with a dashed line.

rapidly by 0.4 dex from 8 to 50 d and then goes down further but slowly by 0.1 dex until 85 d. It is evident from the comparison that the plateau bolometric luminosity of SN 2013ab is close to those of SNe 1999em and 2012aw but with a much steeper decline rate of the light curve during the plateau. However, the decline rate and shape of light curve matches well with that of SN 2004et. The UV–optical bolometric light curve of SN 2013ab also shows a sharp decline by 0.8 dex during the first 50 d, which is steeper than that observed for SN 2012aw. Thereafter, it declines relatively slowly and coincides with the optical light curve. The tail bolometric luminosity is similar to those of SNe 1999em, 2004et and 2012aw, and the slope of the tail is nearly identical to that expected for $^{56}$Co to $^{56}$Fe radioactive decay. Since this powers the tail luminosity, it is directly proportional to the amount of radioactive $^{56}$Ni synthesized during the explosion.

### 4.4 Mass of nickel

The radioactive $^{56}$Ni is produced in CCSNe by the explosive nucleosynthesis of Si to O (Arnett 1980). Thus, the nebular-phase light curve is mainly powered by the radioactive decay of $^{56}$Ni to $^{56}$Co and $^{56}$Co to $^{56}$Fe, with *e*-folding time of 8.8 and 111.26 d, respectively emitting $\gamma$-rays and positrons. Hence, the tail luminosity will be proportional to the amount of synthesized radioactive $^{56}$Ni. The mass of $^{56}$Ni produced by SN 1987A has been determined with a fair degree of accuracy to be 0.075 ± 0.005 M$_\odot$ (Arnett 1996). By comparing the bolometric luminosity of SN 2013ab with that of SN 1987A at similar phases, we can infer the amount of synthesized $^{56}$Ni in SN 2013ab. Although UVOIR bolometric light curve is available for SN 1987A, we preferred to use our *UBVRI* pseudo-bolometric light curve computed using same algorithm that is used for SN 2013ab to have uniformity in the comparison. We estimated the *UBVRI* bolometric luminosity of SN 2013ab at 170 d, by making a linear fit over 160 to 181 d, to be 8.41 ± 0.72 × $10^{40}$ erg s$^{-1}$. Likewise, we estimated the luminosity of SN 1987A at similar phases to be 9.93 ± 0.04 × $10^{40}$ erg s$^{-1}$. The ratio of SN 2013ab to SN 1987A is found to be 0.847 ± 0.073, which gives a $M_{\rm Ni} = 0.064 \pm 0.006$ M$_\odot$ for SN 2013ab.

Assuming the $\gamma$-photons emitted from the radioactive decay of $^{56}$Co thermalize the ejecta, the $^{56}$Ni mass can be independently estimated from the tail luminosity, as described by Hamuy (2003).

$$M_{\rm Ni} = 7.866 \times 10^{-44} \times L_{\rm t} \exp\left[\frac{(t_t - t_0)/(1+z) - 6.1}{111.26}\right] \rm M_\odot,$$

where $t_0$ is the explosion time, 6.1 d is the half-life of $^{56}$Ni and 111.26 d is the e-folding time of the $^{56}$Co decay. We compute the tail luminosity $L_{\rm t}$ at eight epochs between 158 and 182 d from the *V*-band data, corrected for distance, extinction and a bolometric correction factor of 0.26 ± 0.06 mag during nebular phase (Hamuy 2003). The weighted mean value of $L_{\rm t}$ is 18.43 ± 0.83 × $10^{40}$ erg s$^{-1}$, corresponding to a mean phase of 172 d. This tail luminosity corresponds to a value of $M_{\rm Ni} = 0.064 \pm 0.003$ M$_\odot$.

Elmhamdi, Chugai & Danziger (2003b) has found a tight linear correlation between the log($M_{\rm Ni}$) and the plateau *V*-band absolute magnitude at ($t_{\rm i}$ − 35) epoch, where $t_{\rm i}$ is inflection time which is defined as the moment when the slope of the light curve in the transition phase is maximum. For SN 2013ab light curve, we constrained $t_{\rm i}$ = 102.99 ± 0.02 d. Following the above-mentioned correlation, we obtain $M_{\rm Ni} = 0.066 \pm 0.002$ M$_\odot$.

We adopt the mass of synthesized $^{56}$Ni in SN 2013ab to be 0.064 ± 0.006 M$_\odot$, which is derived from the first method, and is found to be consistent with that obtained from the subsequent two

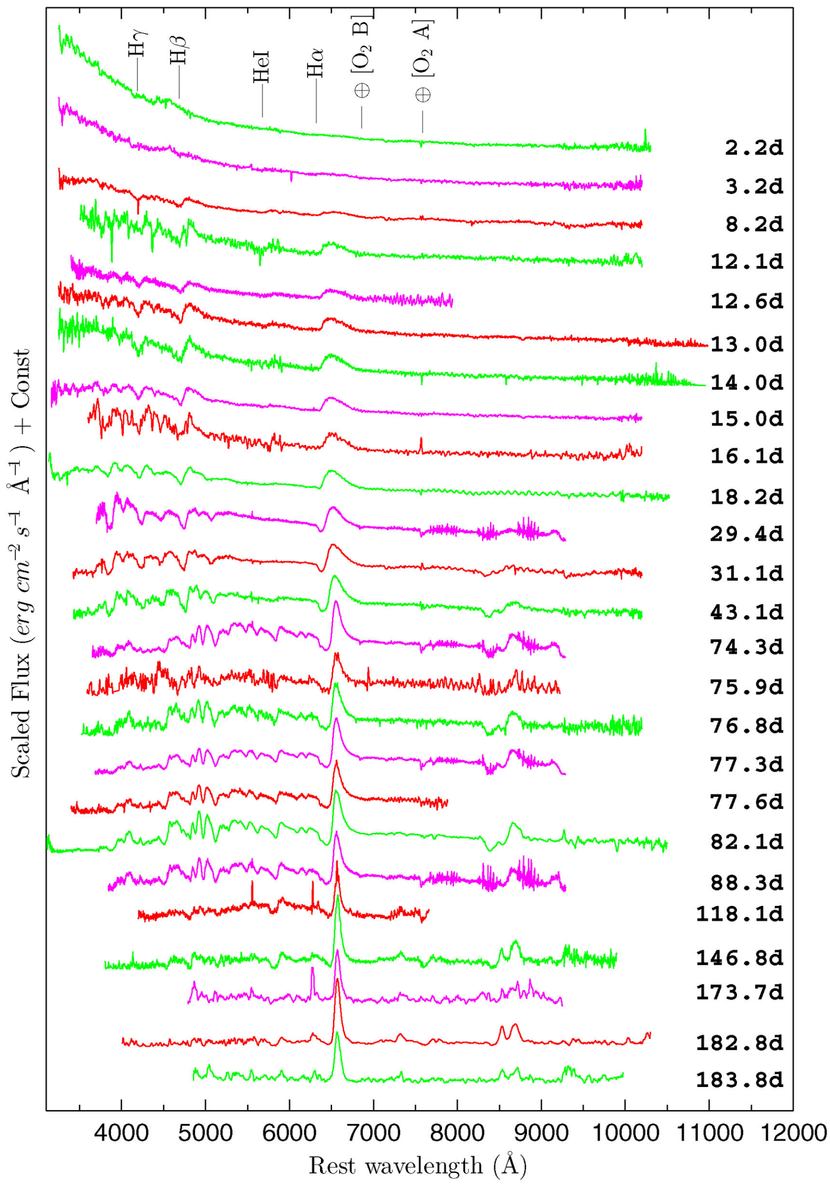


**Figure 9.** The Doppler-corrected spectra of SN 2013ab are shown at 14 phases from 7 to 270 d. Prominent P Cygni profiles of hydrogen (H$\alpha$, H$\beta$, H$\gamma$) and helium (He I $\lambda$5876) lines are marked. The telluric absorption features are indicated with the ⊕ symbol. The portions of spectra at the extreme blue and red ends have poor SNRs.

methods described here. We anticipate that the estimated $^{56}$Ni mass for SN 2013ab is almost equal to that obtained for SNe 2012aw, 2004et and 1999em. Whereas for sub-luminous SN 2005cs, $^{56}$Ni mass is much less than SN 2013ab.

## 5 OPTICAL SPECTRA

### 5.1 Key spectral features

The spectroscopic evolution of SN 2013ab is presented in Fig. 9. Preliminary identification of spectral features has been done as in previous studies of IIP SNe (e.g. Leonard et al. 2002a; Bose et al. 2013). Early spectra, viz. 2.2 d and 3.2 d, shows featureless blue continuum with a broad and shallow P Cygni dip detected near 4380 Å which is supposedly He II $\lambda$4686, which is blueshifted by about 19 500 km s$^{-1}$. Detection of such He II features has been reported in several early SN spectra (Fassia et al. 2001; Quimby et al. 2007; Inserra et al. 2013; Shivvers et al. 2014; Pastorello et al. 2015). The 8.2 d spectrum also primarily shows blue continuum, although with developing H$\beta$, He I and H$\alpha$ lines. The He I feature completely disappears after 18 d and at similar position Na I D profile starts to emerge since the 43 d spectrum.

The spectra from 12 to 18 d mark the transition phase from a hot to cool SN envelope, when photosphere begins to penetrate the deeper Fe-rich ejecta. These spectra mark the emergence of other lines from heavier atomic species, such as calcium, iron, scandium, barium, titanium and neutral sodium. Among these lines, Fe II $\lambda$5169 appear during the early plateau phase (12 d), whereas weaker lines start to emerge at the beginning of late plateau phase (18 d). Na I D doublet $\lambda\lambda$ 5890, 5896 and Ca II triplets $\lambda\lambda$ 8498, 8542, 8662 are feebly traceable from 31 d, and becomes prominent since the 43 d spectrum. All weak and blended lines are seen to evolve and appear

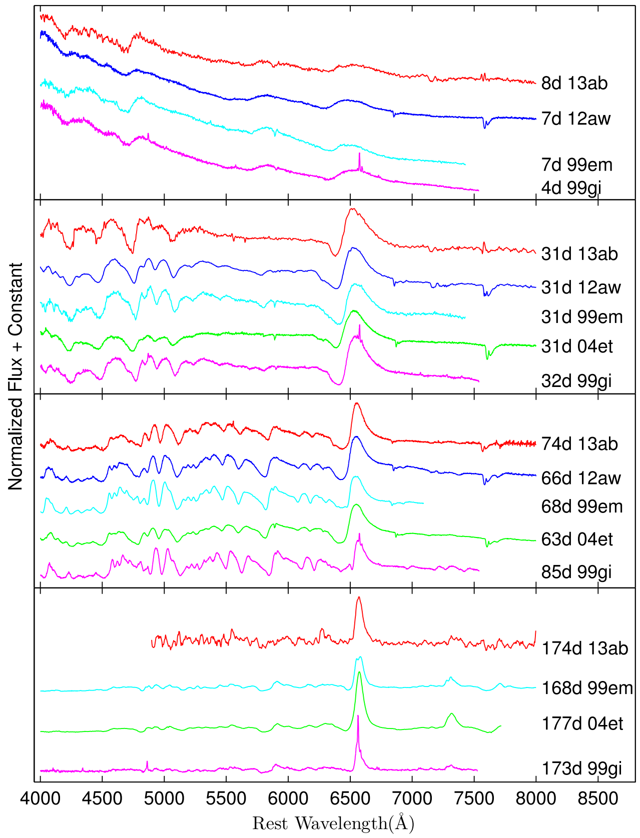


**Figure 10.** Comparison of early (8 d), plateau (31 d, 74 d) and nebular (174 d) phase spectra of SN 2013ab with those of other well-studied Type IIP SNe 2012aw (Bose et al. 2013), 1999em (Leonard et al. 2002a), 1999gi (Leonard et al. 2002b), 2004et (Sahu et al. 2006; Maguire et al. 2010). Observed fluxes of all the SNe are corrected for extinction and redshift (adopted values same as in Fig. 4).

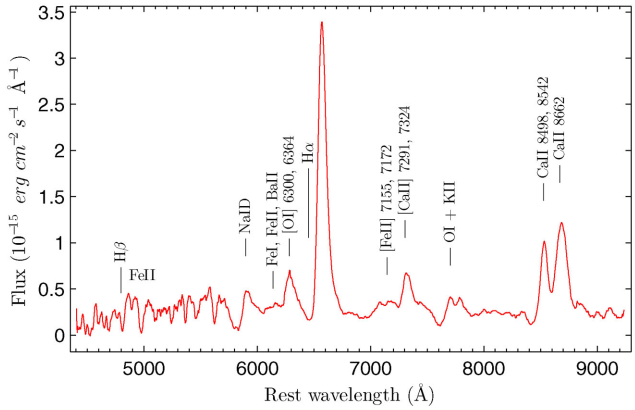


**Figure 11.** Line identification in the nebular phase spectrum of SN 2013ab (183 d).

prominently by the end of plateau phase (82.1 d). The following spectrum (88.3 d) marks the onset of plateau to nebular transition. All subsequent spectra up to 118.1 d are representative of the early nebular phase, when the outer ejecta has become optically thin. Fig. 10 compares SN 2013ab spectra with sample of archetypal IIP events at four different epochs, viz. early and hot plateau phase at 8 d, cooler plateau phase at 31 and 74 d and nebular phase at 174 d. SN 2013ab spectra show features identical to those of our comparison sample of normal events. The nebular spectrum at 183 d is shown in Fig. 11 with preliminary identification of nebular lines typical of SNe IIP. This spectrum is mostly dominated by emission features of [O I] λλ 6300, 6364, [Ca II] λλ 7291, 7324, and [Fe II] λλ 7155, 7172. In addition, permitted emission lines of H I, Na I λλ 5890, 5896 doublet and the Ca II NIR triplet are still detected.

### 5.2 SYNOW modelling of spectra

Spectra of SN 2013ab have been modelled with SYNOW 2.3[2] (Fisher et al. 1997, 1999; Branch et al. 2002) for preliminary line identification and velocity estimates. SYNOW is a parametrized spectrum synthesis code which employs Sobolev approximation to simplify radiation transfer equations, assuming spherically symmetric SN ejecta which expand homologously. Despite of the simplified local thermodynamic equilibrium (LTE) atmosphere assumption in SYNOW, it is capable to produce P Cygni profiles like those produced in the expanding photosphere of an SN. SYNOW has been implemented on several recent SNe studies (e.g. Inserra, Baron & Turatto 2012b; Bose et al. 2013; Milisavljevic et al. 2013; Bose & Kumar 2014; Marion et al. 2014; Takáts et al. 2014) for line identification and estimation of line velocities. We tried three different options for optical depth profiles (viz. Gaussian, exponential and power law), no significant differences were noticed. However, while matching absorption minimum, the exponential profile, $\tau \propto \exp(-v/v_e)$, where $v_e$, a profile fitting parameter, e-folding velocity, was found to be the most suitable and is adopted here for each individual atomic species. One important aspect of SYNOW modelling is the concept of detachment of an ion. When the minimum velocity of a line-forming layer is higher than that of the photospheric layer, the ion is said to be detached, which results into flat topped emission and blueshifted absorption counterpart of the line profile in synthetic spectra produced by SYNOW. This becomes important for H I lines as they are essentially formed at much higher velocities than photospheric velocities. Therefore, only the detached scenario for H I reliably fits the blueshifted absorption trough in the observed spectra.

The observed spectra are dereddened and Doppler-corrected before modelling with SYNOW. $T_{bb}$ is supplied as a model input parameter which is actually the blackbody temperature to produce the underlying LTE continuum of synthetic spectra. For this reason, the observed spectral continuum is well matched at early phases, whereas at later phases this is a poor match with the model as SN emission significantly deviates from LTE assumption. Fig. 12 shows the observed spectrum at 77.3 d with our best-fitting model. A set of atomic species (H I, He I; Fe II; Ti II; Sc II; Ca II; Ba II; Na I; Si II; O I; N I) has been incorporated to generate the synthetic spectrum. The model spectrum can very well reproduce most of the blended line profiles; $v_{ph}$ is optimized to match the Fe II multiplet (λλ 4924, 5018, 5169), whilst the H I velocities are always dealt as a detached scenario.

Line velocities for Hβ, He I and Fe II are estimated from all spectra. The model fit is optimized for velocity locally around the respective lines of interest. Fitting is done locally to avoid any bias in velocity estimation, which may be imposed while accounting for entire spectrum due to other lines at different velocities. In Table 2, SYNOW-estimated velocities for a few representative lines in the plotted spectral sequence are shown. Although Fe II line impression is detectable since 12 d, we model those lines only from

[2] http://www.nhn.ou.edu/~parrent/synow.html

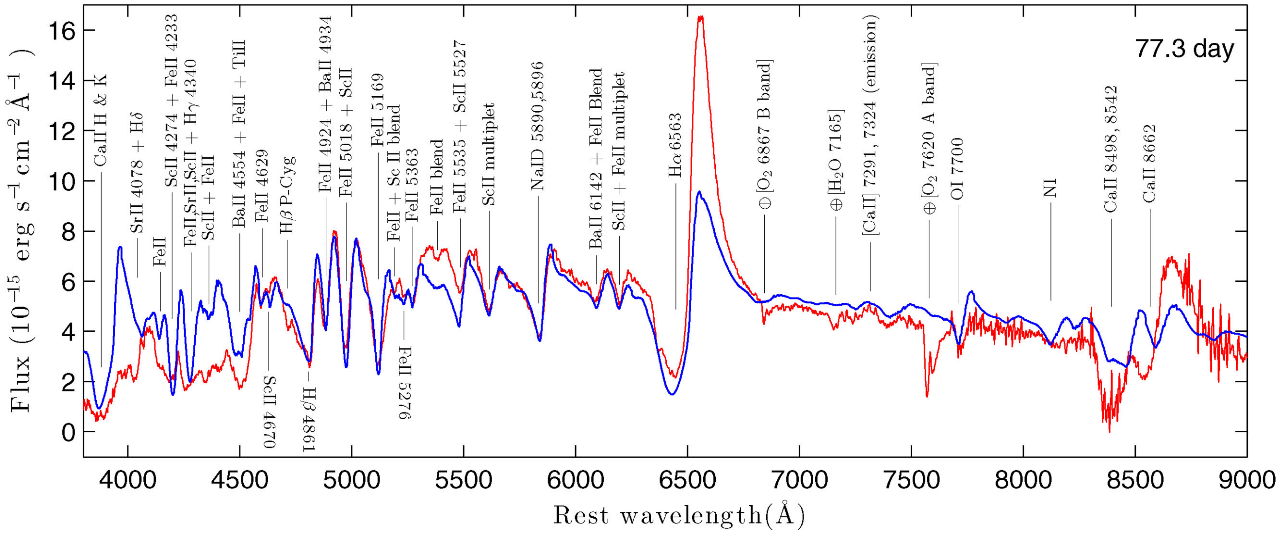


**Figure 12.** SYNOW modelling of the 77.3 d spectrum of SN 2013ab. A SYNOW model spectrum is shown with thick solid line (blue), while the observed one is the thin solid line (red). Fluxes are corrected for interstellar extinction.

**Table 2.** The best-fitting blackbody continuum temperature ($T_{\rm bb}$) and line velocities of H$\beta$, Fe II ($\lambda\lambda$ 4924, 5018, 5169) and He I $\lambda$5876 as estimated from SYNOW modelling of the observed spectra of SN 2013ab. Velocities derived using lines of Fe II or He I are taken as representative of the velocity of photosphere ($v_{\rm ph}$).

| UT Date (yyyy-mm-dd) | Phase[a] (d) | $T^{b}_{\rm bb}$ (kK) | $v$(He I) ($10^3$ km s$^{-1}$) | $v$(Fe II) ($10^3$ km s$^{-1}$) | $v$(H$\beta$) ($10^3$ km s$^{-1}$) |
|---|---|---|---|---|---|
| 2013-02-24.71 | 8.21 | 11.8 | 10.2 ± 0.3 | – | 10.4 ± 0.6 |
| 2013-02-28.59 | 12.09 | 9.6 | 10.1 ± 0.7 | – | 10.4 ± 0.6 |
| 2013-03-01.08 | 12.58 | 1.1 | 9.4 ± 0.4 | – | 10.3 ± 0.3 |
| 2013-03-01.50 | 13.00 | 9.9 | 9.0 ± 0.5 | – | 10.3 ± 0.2 |
| 2013-03-02.51 | 14.01 | 1.0 | 8.7 ± 0.9 | – | 10.2 ± 0.5 |
| 2013-03-03.51 | 15.01 | 9.2 | 9.0 ± 0.6 | – | 9.5 ± 0.2 |
| 2013-03-04.59 | 16.09 | 8.4 | 8.2 ± 0.8 | – | 9.3 ± 0.8 |
| 2013-03-06.71 | 18.21 | 8.5 | 8.3 ± 0.6 | – | 9.8 ± 0.4 |
| 2013-03-17.93 | 29.43 | 6.8 | – | 6.1 ± 0.3 | 7.0 ± 0.3 |
| 2013-03-19.63 | 31.13 | 5.9 | – | 6.5 ± 0.4 | 7.5 ± 0.2 |
| 2013-03-31.58 | 43.08 | 5.6 | – | 4.9 ± 0.4 | 6.0 ± 0.3 |
| 2013-05-01.84 | 74.34 | 5.0 | – | 3.1 ± 0.3 | 3.1 ± 0.4 |
| 2013-05-03.35 | 75.85 | 5.2 | – | – | – |
| 2013-05-04.33 | 76.83 | 5.1 | – | 3.4 ± 0.4 | 3.8 ± 0.3 |
| 2013-05-04.85 | 77.35 | 5.2 | – | 2.9 ± 0.3 | 3.0 ± 0.3 |

*Notes.* [a]With reference to the time of explosion JD 245 6340.0.
[b]Best-fitting blackbody temperature at the photosphere to match the continuum in the observed spectrum.

29 d onwards, as in earlier spectra Fe II triplet is either not full developed or only detectable Fe II $\lambda$5169 is too weak to model. SYNOW modelling is done until 77 d, because after 78 d spectra are limited because of low signal-to-noise ratio (SNR). In such low SNR spectra, SYNOW may not provide any better estimation of line velocities than absorption-minima position measurements.

### 5.3 Evolution of spectral lines

The evolution of spectral features provides important clues about the interaction of expanding ejecta with the circumstellar material, formation of dust in the ejecta and geometrical distribution of the ejecta. To illustrate the evolution of individual lines, in Fig. 13 selected regions of spectra are plotted in the velocity domain corresponding to the rest wavelengths of H$\beta$, Na I D and H$\alpha$. There is no clear evidence of spectral lines in the early spectra (2.2 and 3.2 d), except for a shallow and broad He II ($\lambda$4686) feature near 4380 Å. The blueshifted absorption troughs of the P Cygni profiles give direct estimate of expansion velocity of the ejecta. The emission peaks are also seen to be blueshifted. The amount of blueshift decreases with the decline of the expansion velocity and settles to the rest velocity while the SN enters the nebular phase. This is a generic feature seen in SN spectra, mostly at early phases; see e.g. SNe 1987A (Hanuschik & Dachs 1987), 1998A (Pastorello et al. 2005), 1999em (Elmhamdi et al. 2003a), 2004et (Sahu et al. 2006) and 2012aw (Bose et al. 2013). Blueshifted emission peaks are explained by the diffused reflection of photons from expanding SN envelope (Chugai 1988) which is in contrast to the pure-absorption

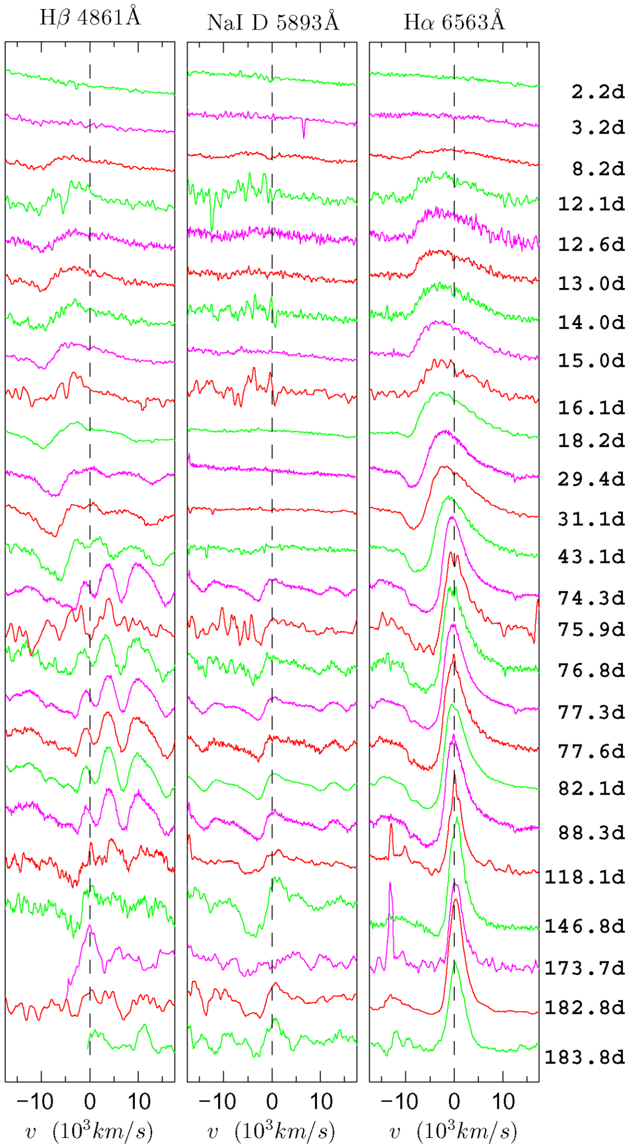


**Figure 13.** Evolution of the line profiles of Hβ, Na I D and Hα plotted at 25 epochs from 2 to 184 d. The zero-velocity position is shown with a dotted line and the corresponding rest wavelength is indicated at the top.

model of expanding atmosphere ensuing unshifted emission peaks. However, recent study by Anderson et al. (2014a) suggests that these features are tied with the density structure of ejecta which in turn controls the amount of occultation of the receding part of ejecta, resulting in biasing of the emission peak. Such features are well reproduced by non-LTE models like CMFGEN (Dessart & Hillier 2005a). The evolution of blueshifted peaks are clearly seen in Hα, whilst other lines emission peaks are heavily contaminated by P Cygni the absorptions from other adjacent lines. The emission peak blueshift for Hα is found to be as high as $\sim\!-5000\,\mathrm{km\,s^{-1}}$at 8.2 d and then progressively decreases ($-4400\,\mathrm{km\,s^{-1}}$ at 12 d and $-2300\,\mathrm{km\,s^{-1}}$at 29.4 d) down to almost zero velocity at 88.3 d, corresponding to the end of plateau phase.

Similar to Hα, Hβ are seen to evolve all throughout the spectral evolution (see Fig. 13). However, 18 d onwards, the red side of Hβ emission profiles are found to be significantly dominated by emerging Fe II lines. All three Fe II lines (λλ 4924, 5018, 5169) are seen to have fully appeared in 31 d spectrum, which continues to evolve till the last observation. Traces of He I line are seen in early spectra, which disappears after 18 d. At similar position, Na I D profile start to appear at 43 d and it continues to evolve until last spectrum.

### 5.4 Ejecta velocity

The element distribution of the progenitor at the end of the sequence of nuclear burnings and before the SN explosion is stratified, with hydrogen being abundant in outermost layers and heavier elements (e.g. α-elements) towards the centre and core being rich in iron. Thus, it is expected that the expanding ejecta are constituted by layers of multiple elements and the so-called onion-like structure. Therefore, different lines originate from different depths in the SN atmosphere. The photosphere is a region of special interest to study the kinematics and other related properties. The photosphere represents the layer of SN atmosphere where optical depth attains a value of ∼2/3 (Dessart & Hillier 2005b). No single spectral line can represent the true photospheric layer and its velocity. During the plateau phase, Fe II (λλ 4924, 5018 and 5169) or Sc II lines are thought to be the best estimators for the photospheric velocity ($v_{\mathrm{ph}}$), and at early phases when Fe II lines are not strongly detected, the best proxy for $v_{\mathrm{ph}}$ is He I or even Hβ (Takáts & Vinkó 2012), at earlier phases.

Velocities can be estimated either by simply locating the blueshifted absorption trough of the P Cygni profiles or modelling the observed spectra where velocity is one of the input parameter. We have used both methods to estimate the velocities. SN spectral lines are often found to be blended with other lines in the neighbourhood, as in the case of Fe II multiplets, blended with Ti II and Ba II. This introduces some error, when lines velocities are estimated by locating the absorption minima, by simply fitting Gaussian function on these blended profiles, which is further exacerbated in low-resolution and low-SNR spectra. SYNOW being capable to reproduce P Cygni profile for multiple lines of different ions simultaneously, it can easily reproduce line blending as observed in SN spectra. Thus, we get a better handle while fitting the entire blended profile with SYNOW and so the velocity estimates are better and less prone to errors. More detailed discussion on applicability and merits of SYNOW velocity estimates over absorption minima method can be found in Takáts & Vinkó (2012) and Bose & Kumar (2014).

In order to estimate photospheric velocities from the model, SYNOW-generated synthetic spectra are locally fitted over Fe II lines in the observed spectra. This was done to avoid any over- or underestimation of velocities as each line of any atomic species originating from different layers. The attributed uncertainties are visually estimated by noting the deviation of model absorption trough from observed one. The model velocities listed in Table 2 are estimated only until 77.3 d, since thereafter the spectra are limited by SNR and hence there is no advantage in using SYNOW-estimated velocities over the absorption minima method. The Fe II velocities are estimated by assuming that the Fe II λ4924, Fe II λ5018, and Fe II λ5169 lines have velocities coincident with $v_{\mathrm{ph}}$, whereas the Balmer H I lines are treated as detached (with $v > v_{\mathrm{ph}}$) (Branch et al. 2002; Bose et al. 2013). He I line velocities have also been estimated as long as this ion can be traced in spectra (from 8.2 to 18.2 d).

The expansion velocities of Hα, Hβ, He I, Fe II (λλ 4924, 5018 and 5169), Sc II λ6247 and Sc II λ4670 have also been determined using IRAF by fitting the absorption trough with a Gaussian profile. The results are plotted in Fig. 14. It can be seen that H I lines are formed at larger radii than He I whereas Fe II lines are formed

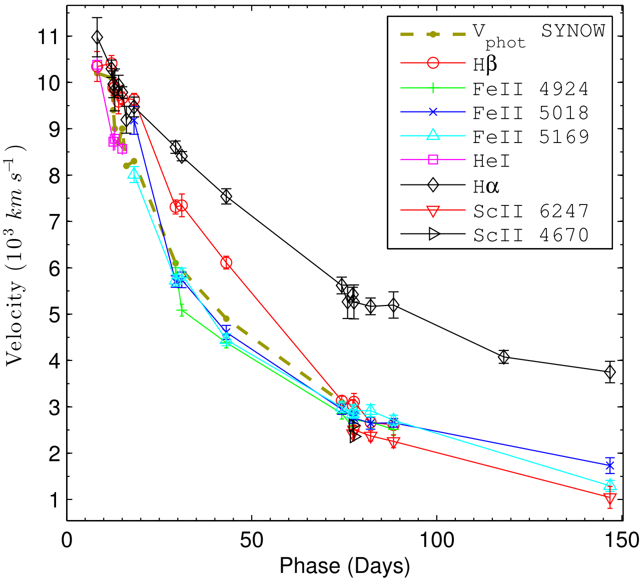


**Figure 14.** Evolution of the H$\alpha$, H$\beta$, He I, Sc II and Fe II line velocities. The velocities are estimated through the Doppler shift of the absorption minima. The expansion velocities at the photosphere ($v_{ph}$) estimated from SYNOW fits of He I line until 18 d and simultaneous fits for Fe II lines at later phases (see Table 2) are shown as a comparison.

at much smaller radii, having lower velocities. The Sc II lines are formed at an even smaller radius. Sc II lines are weak in strength and due to the limitation of our low SNR spectra, these lines are only detected during 77 to 147 d.

Fig. 15 shows the comparison of photospheric velocity of SN 2013ab with those of other well-studied SNe 1987A, 1999em, 1999gi, 2004et, 2005cs and 2012aw. For the purpose of comparison, the absorption trough velocities have been used, taking the mean of Fe II lines (or He I lines at early phases where Fe II lines are not detected). The velocity profile of SN 2013ab is very similar to those of other normal SNe IIP. On the other hand, the velocities of SN 2005cs and SN 1987A are significantly smaller than those of normal events including SN 2013ab. The shape and values of the SN 2013ab velocity profile are strikingly similar to those of SNe 2004et and 2012aw, whereas the velocities are consistently higher than SNe 1999gi and 1999em by ~800 km s$^{-1}$.

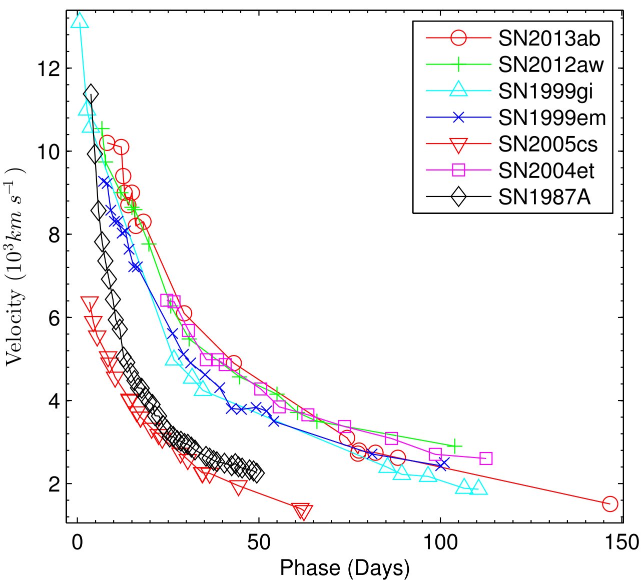


**Figure 15.** The evolution of photospheric velocity ($v_{ph}$) of SN 2013ab is compared with those of other well-studied SNe. The $v_{ph}$ plotted here are the absorption trough velocities (from He I lines at early phases, and Fe II at late phases.)

## 6 EXPANDING PHOTOSPHERE METHOD

EPM is a geometrical technique (Kirshner & Kwan 1974; Eastman, Schmidt & Kirshner 1996) in which the angular radius is compared with physical radius of the SN photosphere to estimate its distance. Assuming homologous expansion of SN photosphere, the physical radius at any instant is approximated from expansion velocity($v_{ph}$), and angular radius ($\theta$) is estimated from blackbody fit corrected with the dilution factor ($\xi$) of Dessart & Hillier (2005b) for non-LTE SNe atmosphere. Distance ($D$) and explosion epoch ($t_0$) are related with the quantity $\theta/v_{ph}$ at any given time $t$ as,

$$t = D\left(\frac{\theta}{v_{ph}}\right) + t_0. \tag{3}$$

Thus, the plot of $t$ against $\theta/v_{ph}$, yield distance as the slope and explosion epoch as the $y$-intercept.

EPM has been successfully applied to a considerably large sample of Type IIP events by Jones et al. (2009) and Bose & Kumar (2014). The merits and limitations of the method have also been tested for multiple aspects. Here, we followed the same approach as described in Bose & Kumar (2014). It has also been shown that the two dilution factor prescriptions given by Hamuy et al. (2001) and Dessart & Hillier (2005c) have significant differences with the latter being more consistent with other redshift-independent distance estimates. In addition, also the SYNOW-estimated velocities are better suited for such analysis. Taking into account all these factors, we have used the Dessart & Hillier (2005c) dilution factor prescription and SYNOW-estimated velocities for EPM analysis. We also restricted our data set up to 30 d only. We derived an EPM distance of 24.26 ± 0.98 Mpc which is the mean value for $BV$, $BVI$ and $VI$ band-sets (Fig. 16). The corresponding derived explosion epoch from EPM is JD 245 6339.59 ± 0.76 d, which is in good agreement with the uncertainty of adopted explosion epoch from

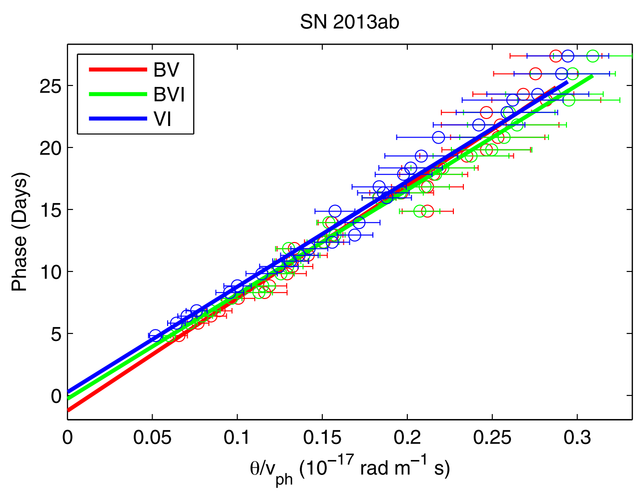


**Figure 16.** The EPM fit for SN 2013ab, using Dessart & Hillier (2005b) prescription for the dilution factor and using three filter sets.

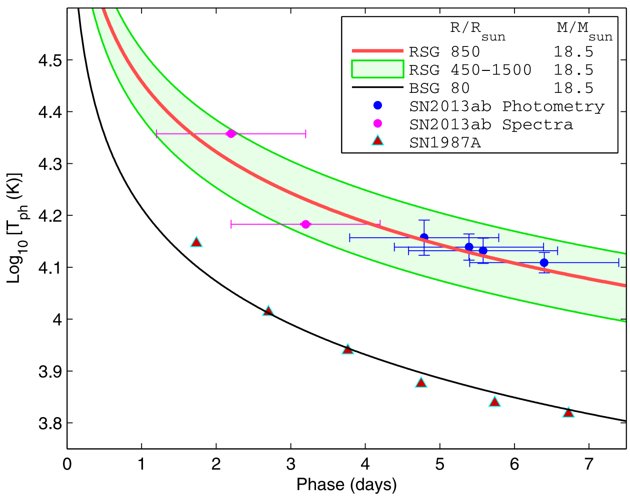


**Figure 17.** Constraining radius using Rabinak & Waxman (2011) prescription. The red solid line is the best fit for RGS of 850 $R_{\odot}$ for SN 2013ab temperatures and the black solid line is for BSG of 80 $R_{\odot}$ for SN 1987A temperatures (Menzies et al. 1987).

observations (see Section 1). In principle, we can constrain explosion epoch and keep distance as the only free parameter for the analysis. This yields a distance of 23.49 ± 0.77 Mpc. Since, the derived explosion epoch from unconstrained analysis is within the uncertainty of the observationally adopted explosion epoch, and the derived distances from constrained and unconstrained analysis are reasonably consistent within the limits of uncertainty, we prefer to adopt the EPM distance as derived from the unconstrained analysis. The EPM distance is found to be in good agreement with mean redshift-independent distance estimates (24.9 ± 5.8 Mpc) listed in NED[3] data base for the galaxy NGC 5669.

## 7 CHARACTERISTICS OF THE EXPLOSION

### 7.1 Radius of progenitor

During the shock breakout, CCSNe heats the envelope to extremely high temperatures and then it cools down as the envelope expands. This temperature evolution depends on several parameters, viz. progenitor radius, opacity, explosion energy and mass. A simplified analytic formulation relating all these parameters has been determined by Rabinak & Waxman (2011). For a progenitor with larger radius, the envelope remains at a higher temperature for a longer time as compared to a progenitor with smaller radius. The temperature evolution is weakly dependent on the progenitor mass and energy, whereas radius and opacity are the dominating parameters. We computed blackbody temperatures from photometric fluxes and spectra and constrained progenitor radius by fitting the relation on these values (Fig. 17). We restricted our fits only within one week of the explosion as the relation is valid for the initial few days after the explosion. We adopted an optical opacity of 0.34 and a typical RSG density profile $f_p = 0.11$; however, it is also noted that results are not very sensitive towards $f_p$. This analysis yields an initial radius of 750–950 $R_{\odot}$ for the progenitor of SN 2013ab, adopting minimal line-of-sight extinction (see Section 3). The radius estimate suggests that the progenitor is possibly a large RSG. With increased extinction value, the estimated radius would increase even further.

### 7.2 Hydrodynamical modelling

With the same well-tested approach adopted for other observed SNe (e.g. SNe 2007od, 2009E, 2009N, 2012A, and 2012aw; see Inserra et al. 2011; Pastorello et al. 2012; Tomasella et al. 2013; Dall'Ora et al. 2014; Takáts et al. 2014), we constrain the main physical properties of SN 2013ab at the explosion (namely the ejected mass, the progenitor radius and the explosion energy) through the hydrodynamical modelling of the main observables (i.e. bolometric light curve, evolution of line velocities and continuum temperature at the photosphere).

According to this approach, a simultaneous $\chi^2$ fit of the above-mentioned observables against model calculations is performed. Two codes are employed for the computation of the models: (1) the first one is the semi-analytic code where the energy balance equation is solved for a homologously expanding envelope of constant density (for details, see Zampieri et al. 2003); (2) the other one is the new general-relativistic, radiation-hydrodynamics Lagrangian code presented in Pumo, Zampieri & Turatto (2010) and Pumo & Zampieri (2011), which is able to simulate the evolution of the physical properties of the CC-SN ejecta and the behaviour of the main observables from the breakout of the shock wave at the stellar surface up to the nebular stage. The distinctive features of this new code are (cf. also Pumo & Zampieri 2013) (a) an accurate treatment of radiative transfer coupled to hydrodynamics, (b) a fully implicit Lagrangian approach to solve the coupled non-linear finite difference system of general-relativistic, radiation-hydrodynamics equations and (c) a description of the evolution of ejected material which takes into account both the gravitational effects of the compact remnant and the heating effects linked to the decay of the radioactive isotopes synthesized during the SN explosion.

The semi-analytic code used to carry out a preparatory study aimed at constraining the parameter space describing the SN progenitor at the explosion. The results of such study are exploited to guide the more realistic, but time consuming model calculations performed with the general-relativistic, radiation-hydrodynamics code.

We note that modelling with both codes is appropriate, since the emission of SN 2013ab is dominated by the expanding ejecta. However, in performing the $\chi^2$ fit, we do not include the observational data taken at early phases (first ∼20–30 d after explosion) because our model is not able to accurately reproduce the early evolution of the main observables, due to the approximate initial density profile used in the simulations which does not precisely reproduce the radial profile of the outermost high-velocity shell of the ejecta forming after the breakout of the shock wave at the stellar surface (cf. Pumo & Zampieri 2011).

The explosion epoch (JD = 245 6340.0) and distance modulus ($\mu = 31.90$ mag) adopted in this paper (see Section 3) are used to fix the explosion epoch and to compute the bolometric luminosity of SN 2013ab, both necessary to perform the comparison with model calculations. Since we do not have IR observations for SN 2013ab, we computed true bolometric luminosity by adding IR contribution, assuming SN 2013ab has similar optical to IR flux ratio as observed for SN 1999em. Adopting a $^{56}$Ni mass of 0.06 $M_{\odot}$ (see Section 4.4), the best-fitting procedure returns values of kinetic plus thermal energy of 0.35 foe, initial radius of 4.2 × $10^{13}$ cm (∼600 $R_{\odot}$) and envelope mass of 7 $M_{\odot}$ (see Fig. 18), with an estimated uncertainty on the modelling parameters of about 15 per cent. Adding the mass

[3] NASA Extragalactic Database: http://ned.ipac.caltech.edu/.

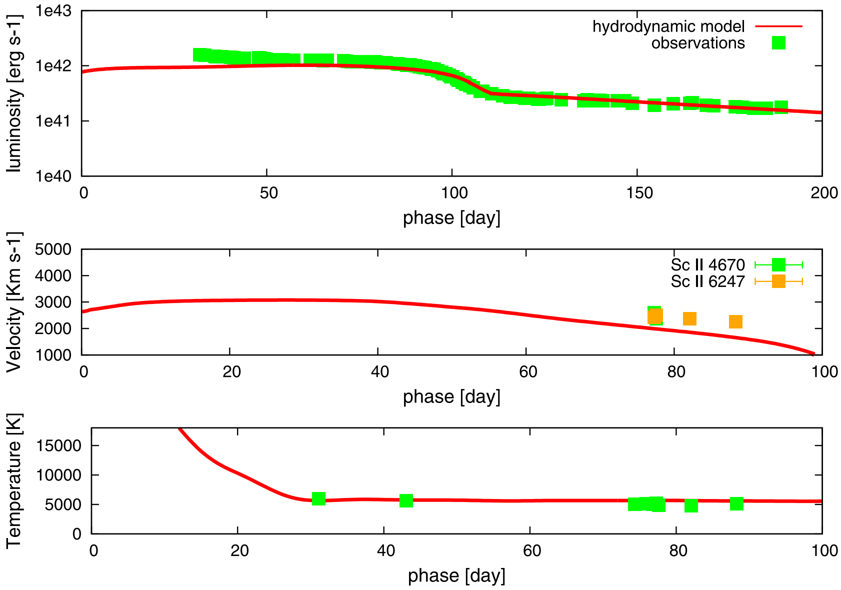


**Figure 18.** Comparison of the evolution of the main observables of SN 2013ab with the best-fitting model computed using the general-relativistic, radiation-hydrodynamics code (total energy 0.35 foe, initial radius $4.2 \times 10^{13}$ cm, envelope mass 7 $M_{\odot}$). Top, middle and bottom panels show the bolometric light curve, the photospheric velocity and the photospheric temperature as a function of time. To better estimate the photosphere velocity from observations, we use the minima of the profile of the Sc II lines which are considered good tracer of the photosphere velocity in Type II SNe. As for the photospheric temperature, we use the blackbody temperature derived from the blackbody fits to the spectral continuum.

of the compact remnant (∼1.5–2.0 $M_{\odot}$) to that of the ejected material, the mass of the progenitor of SN 2013ab at the explosion would be ∼9 $M_{\odot}$.

From the middle panel of Fig. 18, one can note a small (15–20 per cent) discrepancy between the observed photospheric velocity and our best-fitting model. Such discrepancy may be linked to a systematic shift between the true photospheric velocity and the values estimated from the observed P Cygni line profiles (Dessart & Hillier 2005c), according to which the optical depth in the lines could be higher than that in the continuum, causing a shift of the line photosphere to a larger radius (see also Inserra et al. 2013). Nevertheless, we notice that the discrepancy can be eliminated by adopting for the model higher values for the initial radius (∼$6 \times 10^{13}$ cm), the energy (∼0.6 foe) and the envelope mass (up to 13 $M_{\odot}$). However, in this case we get a worse fit to the observed light curve, with a longer (by about 30 per cent) plateau.

The values reported above are consistent with a core collapse scenario from a typical RSG progenitor of relatively low mass. The radius estimate is also consistent within errors with that estimated from early photospheric temperatures described in Section 7.1.

## 8 SUMMARY

In this paper, we present high-cadence broad-band photometric and low-resolution spectroscopic observations of SN 2013ab spanning a duration of about six months. In total, we collected 135 epoch of photometric and 25 epochs of spectroscopic observations. A brief summary of the results obtained in this work is given below.

(i) The light curve and the bolometric luminosity comparisons with other SNe IIP suggest that SN 2013ab is a normal SN IIP, though with a relatively large plateau decline rate (0.92 mag 100 $d^{-1}$ in the *V* band) and a shorter plateau duration (∼78 d). The $^{56}$Ni mass estimated by comparing the tail luminosity with that of SN 1987A yields a value of 0.064 $M_{\odot}$.

(ii) Spectroscopic comparisons show strong resemblance with canonical Type IIP events. Earliest spectra show a featureless continuum. As the SN evolve, the spectra develop metal lines (calcium, iron, scandium, barium, titanium and neutral sodium). Nebular phase spectra show emission lines with little or no P Cygni signatures. Spectra until 77 d with good SNR are modelled using SYNOW to identify most of the prominent features and to estimate expansion velocities for the He I, Fe II and H$\beta$ lines.

(iii) The EPM has been applied to SN 2013ab using the SYNOW-derived velocities and *BVI* photometric data. This provides an independent and reliable estimate of the distance of the galaxy NGC 5669 as 24.3 ± 1.0 Mpc.

(iv) We constrained the physical properties of SN 2013ab at the explosion by means of a hydrodynamical modelling of the main observables which uses the general-relativistic, radiation-hydrodynamics code described in Pumo & Zampieri (2011). The kinetic plus thermal energy is estimated to be ∼0.35 foe, the progenitor mass is ∼9 $M_{\odot}$ and the radius is about 600 $R_{\odot}$.

## ACKNOWLEDGEMENTS

This work makes use of observations from the LCOGT network. We are thankful to the observing and technical staffs of LCOGT, ARIES, HCT and Asiago telescopes for their kind cooperation in observation of SN 2013ab. We gratefully acknowledge the services of the NASA ADS and NED data bases and also the online supernova spectrum archive (SUSPECT) which are used to access data and references in this paper. We acknowledge the TriGrid VL project and the INAF-Astronomical Observatory of Padua for the use of computer facilities. MLP and AP acknowledge the financial support from CSFNSM and from the PRIN-INAF 2011 'Transient

Universe: from ESO Large to PESSTO' (P.I. S. Benetti). We are also thankful to the anonymous referee, whose comments and suggestions has helped in significant improvement of the manuscript.

## REFERENCES


Anderson J. P. et al., 2014a, MNRAS, 441, 671
Anderson J. P. et al., 2014b, ApJ, 786, 67
Arnett W. D., 1980, ApJ, 237, 541
Arnett D., 1996, Supernovae and Nucleosynthesis: An Investigation of the History of Matter from the Big Bang to the Present. Princeton Univ. Press, Princeton, NJ
Barbon R., Benetti S., Rosino L., Cappellaro E., Turatto M., 1990, A&A, 237, 79
Bayless A. J. et al., 2013, ApJ, 764, L13
Bersten M. C., Benvenuto O., Hamuy M., 2011, ApJ, 729, 61
Blanchard P. et al., 2013, Cent. Bur. Electron. Telegrams, 3422, 1
Bose S., Kumar B., 2014, ApJ, 782, 98
Bose S. et al., 2013, MNRAS, 433, 1871
Branch D. et al., 2002, ApJ, 566, 1005
Breeveld A. A., Landsman W., Holland S. T., Roming P., Kuin N. P. M., Page M. J., 2011, in McEnery J. E., Racusin J. L., Gehrels N., eds, AIP Conf. Proc. Vol. 1358, Gamma Ray Bursts 2010. Am. Inst. Phys., New York, p. 373
Brown P. J. et al., 2009, AJ, 137, 4517
Brown T. M. et al., 2013, PASP, 125, 1031
Chugai N. N., 1988, Sov. Astron. Lett., 14, 334
Dall'Ora M. et al., 2014, ApJ, 787, 139
Dessart L., Hillier D. J., 2005a, in Humphreys R., Stanek K., eds, ASP Conf. Ser. Vol. 332, The Fate of the Most Massive Stars. Astron. Soc. Pac., San Francisco, p. 415
Dessart L., Hillier D. J., 2005b, A&A, 437, 667
Dessart L., Hillier D. J., 2005c, A&A, 439, 671
Dessart L., Hillier D. J., 2006, A&A, 447, 691
Dessart L. et al., 2008, ApJ, 675, 644
Eastman R. G., Schmidt B. P., Kirshner R., 1996, ApJ, 466, 911
Elmhamdi A. et al., 2003a, MNRAS, 338, 939
Elmhamdi A., Chugai N. N., Danziger I. J., 2003b, A&A, 404, 1077
Fassia A. et al., 2001, MNRAS, 325, 907
Fisher A., Branch D., Nugent P., Baron E., 1997, ApJ, 481, L89
Fisher A., Branch D., Hatano K., Baron E., 1999, MNRAS, 304, 67
Hamuy M. A., 2001, PhD thesis, Univ. Arizona
Hamuy M., 2003, ApJ, 582, 905
Hamuy M., Suntzeff N. B., 1990, AJ, 99, 1146
Hamuy M., Suntzeff N. B., Heathcote S. R., Walker A. R., Gigoux P., Phillips M. M., 1994, PASP, 106, 566
Hamuy M. et al., 2001, ApJ, 558, 615
Hanuschik R. W., Dachs J., 1987, A&A, 182, L29
Heger A., Fryer C. L., Woosley S. E., Langer N., Hartmann D. H., 2003, ApJ, 591, 288
Horne K., 1986, PASP, 98, 609
Inserra C. et al., 2011, MNRAS, 417, 261
Inserra C. et al., 2012a, MNRAS, 422, 1122
Inserra C., Baron E., Turatto M., 2012b, MNRAS, 422, 1178
Inserra C. et al., 2013, A&A, 555, A142
Jones M. I. et al., 2009, ApJ, 696, 1176
Kasen D., Woosley S. E., 2009, ApJ, 703, 2205
Kirshner R. P., Kwan J., 1974, ApJ, 193, 27
Landolt A. U., 2009, AJ, 137, 4186
Leonard D. C. et al., 2002a, PASP, 114, 35
Leonard D. C. et al., 2002b, AJ, 124, 2490
Maguire K. et al., 2010, MNRAS, 404, 981
Marion G. H. et al., 2014, ApJ, 781, 69
Makarov D., Prugniel P., Terekhova N., Courtois H., Vauglin I., 2014, A&A, 570, A13
Menzies J. W. et al., 1987, MNRAS, 227, 39p
Milisavljevic D. et al., 2013, ApJ, 767, 71
Oke J. B., 1990, AJ, 99, 1621
Olivares E. F. et al., 2010, ApJ, 715, 833
Pastorello A. et al., 2005, MNRAS, 360, 950
Pastorello A. et al., 2009, MNRAS, 394, 2266
Pastorello A. et al., 2012, A&A, 537, A141
Pastorello A. et al., 2015, MNRAS, 449, 1921
Patat F., Barbon R., Cappellaro E., Turatto M., 1994, A&A, 282, 731
Poole T. S. et al., 2008, MNRAS, 383, 627
Pumo M. L., Zampieri L., 2011, ApJ, 741, 41
Pumo M. L., Zampieri L., 2013, MNRAS, 434, 3445
Pumo M. L. et al., 2009, ApJ, 705, L138
Pumo M. L., Zampieri L., Turatto M., 2010, Mem. Soc. Astron. Ital. Suppl., 14, 123
Quimby R. M., Wheeler J. C., Höflich P., Akerlof C. W., Brown P. J., Rykoff E. S., 2007, ApJ, 666, 1093
Rabinak I., Waxman E., 2011, ApJ, 728, 63
Sagar R., Kumar B., Omar A., Joshi Y. C., 2012, Bull. Astron. Soc. India, 4, 173
Sahu D. K., Anupama G. C., Srividya S., Muneer S., 2006, MNRAS, 372, 1315
Schlafly E. F., Finkbeiner D. P., 2011, ApJ, 737, 103
Shivvers I., Mauerhan J. C., Leonard D. C., Filippenko A. V., Fox O. D., 2014, preprint (arXiv:1408.1404)
Smartt S. J., Eldridge J. J., Crockett R. M., Maund J. R., 2009, MNRAS, 395, 1409
Stetson P. B., 1987, PASP, 99, 191
Takáts K., Vinkó J., 2012, MNRAS, 419, 2783
Takáts K. et al., 2014, MNRAS, 438, 368
Theureau G., Hanski M. O., Coudreau N., Hallet N., Martin J. M., 2007, A&A, 465, 71
Tomasella L. et al., 2013, MNRAS, 434, 1636
Tsvetkov D. Y., Goranskij V., Pavlyuk N., 2008, Perem. Zvezdy, 28, 8
Tully R. B., Rizzi L., Shaya E. J., Courtois H. M., Makarov D. I., Jacobs B. A., 2009, AJ, 138, 323
Turatto M., Benetti S., Cappellaro E., 2003, in Hillebrandt W., Leibundgut B., eds, Proc. ESO/MPA/MPE Workshop: From Twilight to Highlight: The Physics of Supernovae. Springer-Verlag, Berlin, p. 200
Utrobin V. P., Chugai N. N., 2009, A&A, 506, 829
Valenti S. et al., 2015, MNRAS, 448, 2608
van Dokkum P. G., 2001, PASP, 113, 1420
Zampieri L., Pastorello A., Turatto M., Cappellaro E., Benetti S., Altavilla G., Mazzali P., Hamuy M., 2003, MNRAS, 338, 711
Zheng W., Blanchard P., Cenko S. B., Filippenko A. V., Cucchiara A., 2013, Astron. Telegram, 4823, 1


## APPENDIX A: PHOTOMETRY

Photometric images were bias-subtracted and flat-fielded, then cosmic ray removal were performed using standard tasks available in IRAF.[4] Due to the position of SN in its host galaxy, we performed point spread function photometry on all frames using DAOPHOT [5] routines. The measured SN flux was significantly affected by the host galaxy flux, therefore an annulus has been chosen conservatively to estimate the host galaxy background.

To calibrate the instrumental light curves of SN 2013ab in *UBVRI*, obtained from ARIES telescopes, four Landolt (2009) standard fields PG 1323, PG 1633, SA 104 and SA 107 were observed

[4] IRAF stands for Image Reduction and Analysis Facility distributed by the National Optical Astronomy Observatories which is operated by the Association of Universities for research in Astronomy, Inc. under cooperative agreement with the National Science Foundation.

[5] DAOPHOT stands for Dominion Astrophysical Observatory Photometry (Stetson 1987).

**Table A1.** Coordinates ($\alpha$, $\delta$) and calibrated magnitudes of secondary standard stars in the field of SN 2013ab. The quoted errors in magnitude include both photometric and calibration errors and it denote $1\sigma$ uncertainty.

Secondary standards used to calibrate *URI* data.

| $\alpha_{J2000}$ (h m s) | $\delta_{J2000}$ (° ′ ″) | $U$ (mag) | $R$ (mag) | $I$ (mag) |
|---|---|---|---|---|
| 14:32:38 | +9:56:39 | 17.654 ± 0.085 | 15.452 ± 0.016 | 14.967 ± 0.014 |
| 14:32:36 | +9:56:00 | 17.406 ± 0.028 | 16.134 ± 0.017 | 15.744 ± 0.016 |
| 14:32:33 | +9:54:45 | 16.968 ± 0.022 | 15.851 ± 0.017 | 15.440 ± 0.016 |
| 14:32:38 | +9:52:24 | 17.709 ± 0.034 | 16.034 ± 0.020 | 15.550 ± 0.021 |
| 14:32:28 | +9:49:43 | 19.362 ± 0.204 | 15.628 ± 0.015 | 14.616 ± 0.015 |
| 14:32:45 | +9:48:37 | 18.118 ± 0.062 | 16.549 ± 0.017 | 16.109 ± 0.020 |
| 14:33:02 | +9:54:41 | 18.789 ± 0.097 | 15.133 ± 0.013 | 14.096 ± 0.015 |
| 14:33:07 | +9:55:52 | 17.354 ± 0.023 | 16.085 ± 0.013 | 15.649 ± 0.013 |
| 14:33:02 | +9:56:03 | 17.828 ± 0.031 | 16.422 ± 0.012 | 15.996 ± 0.014 |
| 14:33:01 | +9:57:25 | 14.520 ± 0.011 | 13.770 ± 0.009 | 13.418 ± 0.013 |
| 14:32:46 | +9:56:10 | 17.918 ± 0.071 | 16.882 ± 0.013 | 16.469 ± 0.015 |

Secondary standards used to calibrate *BVgri* data.

| $\alpha_{J2000}$ (h m s) | $\delta_{J2000}$ (° ′ ″) | $B$ (mag) | $V$ (mag) | $g$ (mag) | $r$ (mag) | $i$ (mag) |
|---|---|---|---|---|---|---|
| 14:32:24 | +9:52:12 | 18.947 ± 0.098 | 18.518 ± 0.032 | 18.749 ± 0.019 | 18.336 ± 0.022 | 18.241 ± 0.026 |
| 14:32:26 | +9:50:09 | 16.924 ± 0.013 | 16.374 ± 0.011 | 16.648 ± 0.011 | 16.147 ± 0.010 | 16.009 ± 0.026 |
| 14:32:32 | +9:47:16 | 17.557 ± 0.040 | 16.977 ± 0.025 | 17.321 ± 0.025 | 16.788 ± 0.016 | 16.629 ± 0.021 |
| 14:32:32 | +9:57:48 | 17.994 ± 0.021 | 17.428 ± 0.016 | 17.733 ± 0.013 | 17.196 ± 0.012 | 17.055 ± 0.022 |
| 14:32:37 | +9:58:48 | 18.937 ± 0.048 | 17.948 ± 0.023 | 18.461 ± 0.019 | 17.413 ± 0.013 | 16.961 ± 0.013 |
| 14:32:40 | +9:45:54 | 14.499 ± 0.016 | 14.064 ± 0.010 | 14.286 ± 0.010 | 13.912 ± 0.010 | 13.814 ± 0.011 |
| 14:32:44 | +9:54:24 | 16.593 ± 0.012 | 15.759 ± 0.010 | 16.166 ± 0.011 | 15.426 ± 0.016 | 15.203 ± 0.023 |
| 14:32:48 | +9:46:33 | 19.776 ± 0.083 | 19.286 ± 0.056 | 19.547 ± 0.057 | 19.189 ± 0.042 | 19.132 ± 0.173 |
| 14:32:59 | +9:45:23 | 17.241 ± 0.021 | 16.804 ± 0.013 | 17.022 ± 0.013 | 16.635 ± 0.012 | 16.497 ± 0.013 |
| 14:33:02 | +9:54:41 | 17.423 ± 0.016 | 16.078 ± 0.011 | 16.746 ± 0.011 | 15.450 ± 0.011 | 14.661 ± 0.010 |
| 14:33:07 | +9:55:52 | 17.096 ± 0.014 | 16.462 ± 0.012 | 16.746 ± 0.011 | 16.216 ± 0.011 | 16.033 ± 0.011 |
| 14:33:11 | +9:59:27 | 17.485 ± 0.015 | 16.674 ± 0.012 | 17.092 ± 0.012 | 16.309 ± 0.011 | 16.042 ± 0.012 |
| 14:33:13 | +9:49:03 | 16.591 ± 0.012 | 16.059 ± 0.011 | 16.329 ± 0.011 | 15.865 ± 0.011 | 15.725 ± 0.011 |
| 14:33:14 | +9:52:02 | 18.502 ± 0.060 | 17.726 ± 0.028 | 18.161 ± 0.016 | 17.349 ± 0.012 | 17.049 ± 0.016 |
| 14:33:15 | +9:51:37 | 15.060 ± 0.012 | 14.534 ± 0.010 | 14.776 ± 0.010 | 14.344 ± 0.010 | 14.230 ± 0.011 |
| 14:33:18 | +9:47:11 | 17.575 ± 0.168 | 17.052 ± 0.062 | 17.586 ± 0.068 | 16.800 ± 0.013 | 16.531 ± 0.014 |

in 2014 March 8 with 104-cm ST under good photometric sky condition with low atmospheric extinction and a typical image FWHM ∼1.9 arcsec in *V* band. Multiple standard fields at different airmasses were used to compute the zero-points, colour coefficients as well as extinction for different filters. In total, 27 standard stars were used for calibration having *V* magnitudes from 11.0 to 15.4. The root-mean-square scatter between standard and the re-calibrated magnitudes of these Landolt stars were found to be ∼0.4 mag in *U*, ∼0.2 mag in *B*, ∼0.1 mag in *V*, *R* and ∼0.3 mag in *I* band. We used the obtained coefficients to standardize 11 non-variable and isolated field stars in the SN frame, which are tabulated in Table. A1. These secondary standards allow us to calibrate the SN light curve obtained using differential photometry. Similarly to standardize the data collected from LCOGT in *BVgri* bands, several secondary standard in the SN field are selected, few of which are also listed in Table. A1. Since, *B* and *V* bands are in common to ARIES and LOCGT data, to have an uniformity we preferred to used LCOGT secondary standards for all *BV* bands data. *Swift*/UVOT data were analysed following the methods described by Poole et al. (2008) and Brown et al. (2009) but adopting the revised zero-points and sensitivity from Breeveld et al. (2011). Template images in all UVOT bands are obtained on 2015 March 13 (755 d), which are used to estimate background fluxes, using same aperture as used for SN measurement. These fluxes are subtracted from SN to eliminate flux contamination due to host galaxy. The final photometry in the *UBVRI*, *gri* and UVOT bands is tabulated in Table A2.

### A1 Photometric data

## APPENDIX B: SPECTROSCOPY

Spectroscopic data were reduced in the IRAF environment. All frames are corrected by bias subtraction and flat-fielding. Cosmic ray rejection on each frame was done using Laplacian kernel detection algorithm for spectra (L.A.Cosmic; van Dokkum 2001). One-dimensional spectra were extracted using *apall* task which is based on optimal extraction algorithm by Horne (1986). Wavelength calibration was performed with the help of the *identify* task by using the arc spectra obtained for all telescopes during each night. The position of O I emission skyline at 5577 Å was used to check the wavelength calibration and deviations were found to lie between 0.3 and 5.5 Å, and this was corrected by applying a linear shift in wavelength.

The flux calibration of wavelength-calibrated spectra was done using *standard, sensfunc* and *calibrate* tasks. We used spectrophotometric standard fluxes from Oke (1990) and Hamuy et al. (1994). All spectra were tied to an absolute flux scale using zero-points determined from *UBVRI* magnitudes. To tie the spectra with

**Table A2.** Photometric evolution of SN 2013ab. Errors denote 1$\sigma$ uncertainty.

| UT Date (yyyy/mm/dd) | JD 245 6000+ | Phase[a] (d) | $U$ (mag) | $B$ (mag) | $V$ (mag) | $R$ (mag) | $I$ (mag) | $g$ (mag) | $r$ (mag) | $i$ (mag) | Tel[b]/ Inst |
|---|---|---|---|---|---|---|---|---|---|---|---|
| 2013-02-15.50 | 339.00 | − 1.00 | – | – | – | – | – | – | > 18.500 | – | 6 |
| 2013-02-17.50 | 341.00 | 1.00 | – | – | – | – | – | – | 17.600 ± 0.095 | – | 6 |
| 2013-02-19.20 | 342.70 | 2.70 | – | – | – | – | – | – | 15.093 ± 0.095 | – | 5 |
| 2013-02-20.29 | 343.79 | 3.79 | – | – | – | – | – | 15.007 ± 0.022 | 15.094 ± 0.047 | 15.297 ± 0.010 | 2,5 |
| 2013-02-20.93 | 344.43 | 4.43 | 14.231 ± 0.040 | – | – | 14.873 ± 0.015 | 14.767 ± 0.030 | – | – | – | 1 |
| 2013-02-21.34 | 344.84 | 4.84 | – | 14.812 ± 0.015 | 14.779 ± 0.012 | – | – | 14.805 ± 0.018 | 14.874 ± 0.011 | 14.956 ± 0.017 | 5 |
| 2013-02-21.57 | 345.07 | 5.07 | – | – | – | – | – | 14.964 ± 0.016 | 14.767 ± 0.068 | 14.994 ± 0.064 | 3 |
| 2013-02-22.34 | 345.84 | 5.84 | – | 14.813 ± 0.015 | 14.747 ± 0.018 | – | – | 14.825 ± 0.018 | 14.759 ± 0.017 | 14.855 ± 0.013 | 5 |
| 2013-02-22.90 | 346.40 | 6.40 | 14.173 ± 0.040 | 14.804 ± 0.025 | – | 14.730 ± 0.014 | 14.586 ± 0.029 | – | – | – | 1 |
| 2013-02-23.34 | 346.84 | 6.84 | – | 14.793 ± 0.013 | 14.705 ± 0.023 | – | – | 14.734 ± 0.028 | 14.744 ± 0.037 | 14.740 ± 0.030 | 5 |
| 2013-02-24.34 | 347.84 | 7.84 | – | 14.793 ± 0.014 | – | – | – | 14.761 ± 0.013 | 14.699 ± 0.010 | 14.763 ± 0.012 | 5 |
| 2013-02-24.80 | 348.30 | 8.30 | 14.231 ± 0.041 | 14.868 ± 0.025 | – | 14.677 ± 0.014 | 14.517 ± 0.030 | – | – | – | 1 |
| 2013-02-25.34 | 348.84 | 8.84 | – | 14.838 ± 0.015 | 14.691 ± 0.019 | – | – | 14.776 ± 0.013 | 14.721 ± 0.025 | 14.776 ± 0.016 | 5 |
| 2013-02-26.34 | 349.84 | 9.84 | – | 14.871 ± 0.011 | 14.729 ± 0.021 | – | – | 14.751 ± 0.020 | 14.717 ± 0.021 | 14.786 ± 0.009 | 5 |
| 2013-02-26.90 | 350.40 | 10.40 | 14.342 ± 0.041 | 14.885 ± 0.025 | – | 14.698 ± 0.014 | 14.552 ± 0.030 | – | – | – | 1 |
| 2013-02-27.34 | 350.84 | 10.84 | – | 14.880 ± 0.014 | 14.783 ± 0.011 | – | – | 14.903 ± 0.013 | 14.685 ± 0.022 | 14.871 ± 0.021 | 5 |
| 2013-02-27.80 | 351.30 | 11.30 | 14.402 ± 0.041 | 14.916 ± 0.025 | – | 14.712 ± 0.014 | 14.580 ± 0.029 | – | – | – | 1 |
| 2013-02-28.34 | 351.84 | 11.84 | – | 14.860 ± 0.015 | 14.814 ± 0.018 | – | – | 14.831 ± 0.016 | 14.741 ± 0.014 | 14.822 ± 0.015 | 5 |
| 2013-02-28.86 | 352.36 | 12.36 | 14.497 ± 0.040 | 14.974 ± 0.025 | – | 14.733 ± 0.014 | 14.612 ± 0.029 | – | – | – | 1 |
| 2013-03-01.44 | 352.94 | 12.94 | – | 15.018 ± 0.005 | 14.901 ± 0.006 | – | – | 14.935 ± 0.005 | 14.809 ± 0.005 | 14.911 ± 0.009 | 5 |
| 2013-03-02.44 | 353.94 | 13.94 | – | 14.950 ± 0.006 | 14.889 ± 0.010 | – | – | 14.925 ± 0.007 | 14.777 ± 0.009 | 14.934 ± 0.009 | 5 |
| 2013-03-03.39 | 354.89 | 14.89 | – | 15.092 ± 0.017 | 14.826 ± 0.018 | – | – | 14.917 ± 0.003 | 14.798 ± 0.006 | 14.951 ± 0.007 | 5 |
| 2013-03-04.44 | 355.94 | 15.94 | – | 15.046 ± 0.005 | 14.920 ± 0.005 | – | – | 14.957 ± 0.005 | 14.802 ± 0.005 | 14.945 ± 0.009 | 5 |
| 2013-03-04.84 | 356.34 | 16.34 | 14.715 ± 0.040 | 15.073 ± 0.025 | – | 14.770 ± 0.014 | 14.668 ± 0.029 | – | – | – | 1 |
| 2013-03-05.32 | 356.82 | 16.82 | – | 15.102 ± 0.023 | 14.885 ± 0.018 | – | – | 14.972 ± 0.015 | 14.753 ± 0.024 | 14.893 ± 0.027 | 5 |
| 2013-03-06.32 | 357.82 | 17.82 | – | 15.122 ± 0.012 | 14.905 ± 0.021 | – | – | 15.007 ± 0.019 | 14.750 ± 0.026 | 14.930 ± 0.023 | 5 |
| 2013-03-06.85 | 358.35 | 18.35 | 14.879 ± 0.040 | 15.124 ± 0.025 | – | 14.768 ± 0.014 | 14.652 ± 0.029 | – | – | – | 1 |
| 2013-03-07.82 | 359.32 | 19.32 | 14.951 ± 0.040 | 15.162 ± 0.025 | – | 14.762 ± 0.014 | 14.642 ± 0.029 | – | – | – | 1 |
| 2013-03-08.31 | 359.81 | 19.81 | – | 15.198 ± 0.017 | – | – | – | – | – | – | 5 |
| 2013-03-09.36 | 360.86 | 20.86 | – | 15.196 ± 0.016 | 14.886 ± 0.012 | – | – | 15.026 ± 0.009 | 14.783 ± 0.009 | – | 5 |
| 2013-03-10.35 | 361.85 | 21.85 | – | 15.254 ± 0.016 | 14.935 ± 0.026 | – | – | 15.075 ± 0.012 | 14.832 ± 0.013 | 14.934 ± 0.015 | 5 |
| 2013-03-11.33 | 362.83 | 22.83 | – | 15.236 ± 0.010 | 14.963 ± 0.014 | – | – | 15.067 ± 0.016 | 14.814 ± 0.019 | 14.939 ± 0.021 | 5 |
| 2013-03-12.37 | 363.87 | 23.87 | – | 15.363 ± 0.016 | 14.952 ± 0.019 | – | – | 15.091 ± 0.014 | 14.827 ± 0.004 | 14.923 ± 0.004 | 5 |
| 2013-03-12.80 | 364.30 | 24.30 | 15.503 ± 0.041 | 15.354 ± 0.025 | 14.994 ± 0.012 | 14.756 ± 0.014 | 14.605 ± 0.029 | – | – | – | 1 |
| 2013-03-14.44 | 365.94 | 25.94 | – | 15.422 ± 0.012 | 15.036 ± 0.013 | – | – | 15.202 ± 0.011 | 14.890 ± 0.015 | 14.985 ± 0.018 | 5 |
| 2013-03-15.88 | 367.38 | 27.38 | 15.819 ± 0.042 | 15.486 ± 0.025 | 15.056 ± 0.012 | 14.793 ± 0.014 | 14.636 ± 0.029 | – | – | – | 1 |
| 2013-03-19.94 | 371.44 | 31.44 | 16.145 ± 0.044 | 15.665 ± 0.025 | 15.166 ± 0.012 | 14.867 ± 0.014 | 14.693 ± 0.029 | – | – | – | 1 |
| 2013-03-20.44 | 371.94 | 31.94 | – | 15.695 ± 0.007 | 15.113 ± 0.005 | – | – | 15.383 ± 0.003 | 14.934 ± 0.004 | 15.035 ± 0.007 | 5 |
| 2013-03-21.71 | 373.21 | 33.21 | 16.243 ± 0.053 | – | 15.203 ± 0.013 | 14.900 ± 0.015 | 14.692 ± 0.031 | – | – | – | 1 |
| 2013-03-24.43 | 375.93 | 35.93 | – | 15.812 ± 0.010 | 15.230 ± 0.007 | – | – | 15.464 ± 0.005 | 15.003 ± 0.005 | – | 5 |
| 2013-03-24.90 | 376.40 | 36.40 | – | 15.848 ± 0.027 | 15.248 ± 0.013 | 14.927 ± 0.014 | – | – | – | – | 1 |
| 2013-03-25.75 | 377.25 | 37.25 | 16.633 ± 0.059 | 15.866 ± 0.027 | 15.257 ± 0.009 | 14.936 ± 0.015 | 14.718 ± 0.030 | – | – | – | 1 |
| 2013-03-26.38 | 377.88 | 37.88 | – | 15.911 ± 0.012 | 15.245 ± 0.012 | – | – | – | – | – | 5 |
| 2013-03-28.81 | 380.31 | 40.31 | 16.681 ± 0.062 | 15.968 ± 0.028 | 15.282 ± 0.013 | 14.966 ± 0.015 | 14.729 ± 0.030 | – | – | – | 1 |
| 2013-03-29.78 | 381.28 | 41.28 | 16.814 ± 0.104 | 15.982 ± 0.029 | 15.303 ± 0.013 | 14.971 ± 0.014 | 14.722 ± 0.030 | – | – | – | 1 |

**Table A2** – *continued*

| UT Date (yyyy/mm/dd) | JD 245 6000+ | Phase[a] (d) | *U* (mag) | *B* (mag) | *V* (mag) | *R* (mag) | *I* (mag) | *g* (mag) | *r* (mag) | *i* (mag) | Tel[b]/ Inst |
|---|---|---|---|---|---|---|---|---|---|---|---|
| 2013-03-30.87 | 382.37 | 42.37 | 16.910 ± 0.066 | 16.035 ± 0.027 | 15.316 ± 0.013 | 14.997 ± 0.015 | 14.763 ± 0.029 | – | – | – | 1 |
| 2013-04-01.38 | 383.88 | 43.88 | – | 16.068 ± 0.013 | 15.278 ± 0.014 | – | – | 15.619 ± 0.014 | 15.073 ± 0.017 | 15.083 ± 0.018 | 5 |
| 2013-04-05.39 | 387.89 | 47.89 | – | 16.073 ± 0.204 | 15.277 ± 0.025 | – | – | 15.640 ± 0.020 | 15.064 ± 0.026 | 15.074 ± 0.028 | 5 |
| 2013-04-05.83 | 388.33 | 48.33 | 17.143 ± 0.055 | 16.074 ± 0.026 | 15.307 ± 0.012 | 14.986 ± 0.014 | 14.736 ± 0.029 | – | – | – | 1 |
| 2013-04-06.40 | 388.90 | 48.90 | – | 16.183 ± 0.030 | – | – | – | – | – | – | 5 |
| 2013-04-06.85 | 389.35 | 49.35 | 17.200 ± 0.042 | 16.087 ± 0.018 | 15.317 ± 0.008 | 15.117 ± 0.010 | 14.731 ± 0.021 | – | – | – | 1 |
| 2013-04-07.39 | 389.89 | 49.89 | – | 16.203 ± 0.010 | 15.340 ± 0.012 | – | – | 15.693 ± 0.013 | 15.110 ± 0.014 | 15.119 ± 0.012 | 5 |
| 2013-04-10.88 | 393.38 | 53.38 | 17.429 ± 0.047 | 16.243 ± 0.026 | 15.381 ± 0.012 | 15.032 ± 0.014 | 14.751 ± 0.029 | – | – | – | 1 |
| 2013-04-11.85 | 394.35 | 54.35 | 17.487 ± 0.073 | 16.243 ± 0.026 | 15.383 ± 0.012 | 15.030 ± 0.014 | 14.748 ± 0.029 | – | – | – | 1 |
| 2013-04-14.36 | 396.86 | 56.86 | – | 16.362 ± 0.011 | 15.372 ± 0.010 | – | – | 15.771 ± 0.008 | 15.167 ± 0.008 | 15.194 ± 0.009 | 5 |
| 2013-04-14.77 | 397.27 | 57.27 | 17.522 ± 0.052 | 16.288 ± 0.026 | 15.403 ± 0.012 | 15.042 ± 0.014 | 14.761 ± 0.029 | – | – | – | 1 |
| 2013-04-19.32 | 401.82 | 61.82 | – | 16.402 ± 0.014 | 15.373 ± 0.011 | – | – | 15.838 ± 0.007 | 15.197 ± 0.010 | 15.122 ± 0.013 | 5 |
| 2013-04-20.32 | 402.82 | 62.82 | – | 16.390 ± 0.012 | 15.420 ± 0.010 | – | – | 15.804 ± 0.006 | 15.229 ± 0.009 | 15.191 ± 0.012 | 5 |
| 2013-04-21.32 | 403.82 | 63.82 | – | 16.444 ± 0.018 | 15.387 ± 0.014 | – | – | 15.793 ± 0.013 | 15.153 ± 0.018 | 15.150 ± 0.016 | 5 |
| 2013-04-22.77 | 405.27 | 65.27 | 17.637 ± 0.098 | 16.415 ± 0.022 | 15.430 ± 0.009 | 15.061 ± 0.016 | 14.787 ± 0.030 | – | – | – | 1 |
| 2013-04-23.32 | 405.82 | 65.82 | – | 16.330 ± 0.026 | 15.411 ± 0.012 | – | – | 15.820 ± 0.014 | 15.182 ± 0.019 | 15.143 ± 0.017 | 5 |
| 2013-04-23.80 | 406.30 | 66.30 | – | – | 15.422 ± 0.017 | 15.084 ± 0.015 | 14.781 ± 0.030 | – | – | – | 1 |
| 2013-04-26.28 | 408.78 | 68.78 | – | – | – | – | – | 15.874 ± 0.018 | 15.099 ± 0.016 | – | 5 |
| 2013-04-28.28 | 410.78 | 70.78 | – | 16.480 ± 0.019 | 15.406 ± 0.014 | – | – | 15.818 ± 0.011 | 15.129 ± 0.016 | 15.137 ± 0.016 | 5 |
| 2013-04-29.28 | 411.78 | 71.78 | – | 16.520 ± 0.014 | 15.437 ± 0.011 | – | – | 15.858 ± 0.009 | 15.187 ± 0.008 | 15.175 ± 0.012 | 5 |
| 2013-04-30.28 | 412.78 | 72.78 | – | 16.557 ± 0.013 | 15.486 ± 0.012 | – | – | 15.889 ± 0.011 | 15.227 ± 0.010 | 15.246 ± 0.013 | 5 |
| 2013-05-01.77 | 414.27 | 74.27 | 17.740 ± 0.053 | – | 15.444 ± 0.013 | 15.086 ± 0.014 | 14.792 ± 0.030 | – | – | – | 1 |
| 2013-05-03.27 | 415.77 | 75.77 | – | 16.617 ± 0.025 | 15.498 ± 0.015 | – | – | 15.885 ± 0.011 | 15.231 ± 0.012 | – | 5 |
| 2013-05-05.75 | 418.25 | 78.25 | 17.841 ± 0.094 | – | 15.466 ± 0.012 | 15.107 ± 0.014 | 14.820 ± 0.021 | – | – | – | 1 |
| 2013-05-06.76 | 419.26 | 79.26 | 17.920 ± 0.086 | – | 15.457 ± 0.012 | 15.094 ± 0.014 | 14.802 ± 0.029 | – | – | – | 1 |
| 2013-05-08.27 | 420.77 | 80.77 | – | 16.620 ± 0.027 | 15.562 ± 0.019 | – | – | 15.985 ± 0.015 | 15.298 ± 0.013 | 15.224 ± 0.021 | 5 |
| 2013-05-08.79 | 421.29 | 81.29 | 18.113 ± 0.061 | – | 15.494 ± 0.012 | 15.123 ± 0.015 | 14.815 ± 0.030 | – | – | – | 1 |
| 2013-05-09.72 | 422.22 | 82.22 | 18.070 ± 0.057 | – | 15.510 ± 0.009 | 15.119 ± 0.015 | 14.823 ± 0.030 | – | – | – | 1 |
| 2013-05-12.74 | 425.24 | 85.24 | 18.069 ± 0.078 | – | 15.567 ± 0.013 | 15.174 ± 0.015 | 14.815 ± 0.032 | – | – | – | 1 |
| 2013-05-13.24 | 425.74 | 85.74 | – | 16.793 ± 0.023 | 15.621 ± 0.015 | – | – | 16.084 ± 0.010 | 15.360 ± 0.011 | 15.329 ± 0.014 | 5 |
| 2013-05-15.24 | 427.74 | 87.74 | – | 16.874 ± 0.021 | 15.653 ± 0.014 | – | – | 16.127 ± 0.010 | 15.360 ± 0.009 | 15.349 ± 0.013 | 5 |
| 2013-05-16.26 | 428.76 | 88.76 | – | 16.827 ± 0.021 | 15.597 ± 0.013 | – | – | 16.093 ± 0.015 | 15.337 ± 0.012 | – | 5 |
| 2013-05-17.74 | 430.24 | 90.24 | 18.634 ± 0.147 | – | 15.668 ± 0.013 | 15.223 ± 0.014 | 14.926 ± 0.030 | – | – | – | 1 |
| 2013-05-18.71 | 431.21 | 91.21 | – | – | 15.718 ± 0.010 | 15.279 ± 0.015 | 14.969 ± 0.031 | – | – | – | 1 |
| 2013-05-19.69 | 432.19 | 92.19 | – | – | 15.740 ± 0.015 | 15.298 ± 0.016 | 14.978 ± 0.031 | – | – | – | 1 |
| 2013-05-20.26 | 432.76 | 92.76 | – | 17.002 ± 0.021 | 15.764 ± 0.015 | – | – | 16.256 ± 0.021 | 15.474 ± 0.027 | 15.425 ± 0.025 | 5 |
| 2013-05-21.72 | 434.22 | 94.22 | – | – | 15.783 ± 0.015 | 15.350 ± 0.012 | 15.025 ± 0.034 | – | – | – | 1 |
| 2013-05-22.23 | 434.73 | 94.73 | – | 17.154 ± 0.034 | 15.864 ± 0.014 | – | – | 16.382 ± 0.013 | 15.523 ± 0.016 | 15.466 ± 0.020 | 5 |
| 2013-05-22.72 | 435.22 | 95.22 | – | 17.002 ± 0.030 | 15.850 ± 0.011 | 15.390 ± 0.012 | 15.048 ± 0.023 | – | – | – | 1 |
| 2013-05-23.73 | 436.23 | 96.23 | – | 17.075 ± 0.047 | 15.950 ± 0.022 | 15.456 ± 0.019 | 15.129 ± 0.034 | – | – | – | 1 |
| 2013-05-24.74 | 437.24 | 97.24 | – | 17.191 ± 0.062 | 16.017 ± 0.022 | 15.543 ± 0.020 | 15.204 ± 0.037 | – | – | – | 1 |
| 2013-05-25.23 | 437.73 | 97.73 | – | 17.383 ± 0.125 | 16.092 ± 0.044 | – | – | 16.621 ± 0.052 | 15.738 ± 0.047 | 15.605 ± 0.033 | 5 |
| 2013-05-25.83 | 438.33 | 98.33 | – | 17.213 ± 0.089 | 16.081 ± 0.032 | 15.613 ± 0.021 | 15.270 ± 0.036 | – | – | – | 1 |
| 2013-05-26.72 | 439.22 | 99.22 | – | 17.417 ± 0.040 | 16.191 ± 0.015 | 15.677 ± 0.017 | 15.293 ± 0.033 | – | – | – | 1 |
| 2013-05-27.23 | 439.73 | 99.73 | – | 17.671 ± 0.021 | 16.264 ± 0.011 | – | – | 16.816 ± 0.008 | 15.842 ± 0.010 | 15.749 ± 0.010 | 5 |

**Table A2** – *continued*

| UT Date (yyyy/mm/dd) | JD 245 6000+ | Phase[a] (d) | *U* (mag) | *B* (mag) | *V* (mag) | *R* (mag) | *I* (mag) | *g* (mag) | *r* (mag) | *i* (mag) | Tel[b]/ Inst |
|---|---|---|---|---|---|---|---|---|---|---|---|
| 2013-05-27.70 | 440.20 | 100.20 | 18.856 ± 0.355 | 17.505 ± 0.037 | 16.254 ± 0.014 | 15.729 ± 0.017 | 15.335 ± 0.032 | – | – | – | 1 |
| 2013-05-28.76 | 441.26 | 101.26 | 18.513 ± 0.293 | 17.638 ± 0.038 | 16.382 ± 0.014 | 15.829 ± 0.019 | 15.417 ± 0.033 | – | – | – | 1 |
| 2013-05-29.23 | 441.73 | 101.73 | – | 17.841 ± 0.024 | 16.517 ± 0.029 | – | – | 17.030 ± 0.011 | 16.018 ± 0.008 | 15.922 ± 0.014 | 5 |
| 2013-05-30.23 | 442.73 | 102.73 | – | 18.019 ± 0.021 | 16.605 ± 0.014 | – | – | 17.199 ± 0.014 | 16.128 ± 0.011 | 16.017 ± 0.010 | 5 |
| 2013-05-30.80 | 443.30 | 103.30 | – | 17.844 ± 0.038 | 16.594 ± 0.015 | 16.004 ± 0.017 | – | – | – | – | 1 |
| 2013-05-31.24 | 443.74 | 103.74 | – | 18.170 ± 0.039 | 16.736 ± 0.020 | – | – | 17.345 ± 0.015 | 16.241 ± 0.013 | – | 5 |
| 2013-06-01.23 | 444.73 | 104.73 | – | 18.259 ± 0.025 | 16.800 ± 0.018 | – | – | 17.422 ± 0.012 | 16.289 ± 0.010 | 16.204 ± 0.020 | 5 |
| 2013-06-02.23 | 445.73 | 105.73 | – | 18.485 ± 0.051 | 16.894 ± 0.027 | – | – | 17.548 ± 0.018 | 16.370 ± 0.015 | 16.256 ± 0.023 | 5 |
| 2013-06-04.18 | 447.68 | 107.68 | – | 18.599 ± 0.046 | 17.113 ± 0.023 | – | – | 17.734 ± 0.021 | 16.529 ± 0.017 | 16.411 ± 0.022 | 5 |
| 2013-06-04.78 | 448.28 | 108.28 | – | – | 17.048 ± 0.020 | 16.399 ± 0.022 | – | – | – | – | 1 |
| 2013-06-07.18 | 450.68 | 110.68 | – | 18.700 ± 0.047 | 17.207 ± 0.029 | – | – | 17.888 ± 0.022 | 16.744 ± 0.018 | 16.619 ± 0.026 | 5 |
| 2013-06-10.22 | 453.72 | 113.72 | – | 18.806 ± 0.084 | 17.278 ± 0.031 | – | – | 17.962 ± 0.025 | 16.715 ± 0.026 | 16.691 ± 0.036 | 5 |
| 2013-06-12.22 | 455.72 | 115.72 | – | – | 17.316 ± 0.028 | – | – | 18.003 ± 0.024 | 16.794 ± 0.021 | 16.651 ± 0.030 | 5 |
| 2013-06-12.68 | 456.18 | 116.18 | 19.743 ± 0.527 | – | 17.291 ± 0.031 | 16.632 ± 0.025 | 16.146 ± 0.037 | – | – | – | 1 |
| 2013-06-13.72 | 457.22 | 117.22 | 19.625 ± 0.411 | – | 17.293 ± 0.023 | 16.627 ± 0.024 | 16.161 ± 0.036 | – | – | – | 1 |
| 2013-06-16.13 | 459.63 | 119.63 | – | 18.911 ± 0.044 | 17.414 ± 0.018 | – | – | 18.053 ± 0.042 | 16.806 ± 0.017 | 16.727 ± 0.024 | 5 |
| 2013-06-17.20 | 460.70 | 120.70 | – | 18.885 ± 0.038 | 17.362 ± 0.110 | – | – | – | – | – | 5 |
| 2013-06-19.72 | 463.22 | 123.22 | – | – | 17.446 ± 0.036 | 16.749 ± 0.026 | 16.292 ± 0.038 | – | – | – | 1 |
| 2013-06-20.10 | 463.60 | 123.60 | – | – | 17.478 ± 0.026 | – | – | 18.052 ± 0.020 | – | – | 5 |
| 2013-06-21.73 | 465.23 | 125.23 | – | – | 17.463 ± 0.053 | 16.700 ± 0.034 | 16.245 ± 0.045 | – | – | – | 1 |
| 2013-06-22.05 | 465.55 | 125.55 | – | 18.790 ± 0.065 | 17.454 ± 0.021 | – | – | 18.007 ± 0.021 | 16.851 ± 0.012 | 16.794 ± 0.022 | 5 |
| 2013-06-24.05 | 467.55 | 127.55 | – | 19.004 ± 0.086 | – | – | – | 18.032 ± 0.018 | 16.901 ± 0.013 | 16.770 ± 0.015 | 5 |
| 2013-06-26.05 | 469.55 | 129.55 | – | 18.950 ± 0.048 | 17.519 ± 0.018 | – | – | 18.091 ± 0.015 | 16.896 ± 0.011 | 16.851 ± 0.015 | 5 |
| 2013-07-02.06 | 475.56 | 135.56 | – | 18.963 ± 0.029 | 17.623 ± 0.018 | – | – | 18.190 ± 0.014 | 16.912 ± 0.012 | 16.898 ± 0.013 | 5 |
| 2013-07-03.06 | 476.56 | 136.56 | – | 18.936 ± 0.032 | 17.533 ± 0.021 | – | – | – | 16.880 ± 0.017 | 16.911 ± 0.024 | 5 |
| 2013-07-04.21 | 477.71 | 137.71 | – | 18.933 | – | – | – | – | – | 16.990 ± 0.022 | 5 |
| 2013-07-05.21 | 478.71 | 138.71 | – | 19.027 ± 0.052 | 17.588 ± 0.020 | – | – | 18.178 ± 0.024 | 16.956 ± 0.011 | 16.937 ± 0.014 | 5 |
| 2013-07-06.21 | 479.71 | 139.71 | – | 18.875 ± 0.052 | 17.579 ± 0.026 | – | – | 18.168 ± 0.020 | 16.983 ± 0.015 | 16.965 ± 0.021 | 5 |
| 2013-07-07.19 | 480.69 | 140.69 | – | 18.936 ± 0.068 | 17.624 ± 0.035 | – | – | 18.188 ± 0.022 | 16.952 ± 0.020 | 16.952 ± 0.017 | 5 |
| 2013-07-11.15 | 484.65 | 144.65 | – | 18.865 ± 0.050 | 17.611 ± 0.024 | – | – | 18.185 ± 0.019 | 16.968 ± 0.017 | 17.067 ± 0.020 | 5 |
| 2013-07-13.15 | 486.65 | 146.65 | – | 18.910 ± 0.050 | 17.604 ± 0.028 | – | – | 18.206 ± 0.016 | 16.993 ± 0.014 | 17.026 ± 0.019 | 5 |
| 2013-07-15.18 | 488.68 | 148.68 | – | – | 17.773 ± 0.066 | – | – | 18.258 ± 0.078 | 17.089 ± 0.045 | – | 5 |
| 2013-07-21.18 | 494.68 | 154.68 | – | 19.072 ± 0.111 | 17.914 ± 0.043 | – | – | 18.240 ± 0.034 | 17.047 ± 0.021 | 17.215 ± 0.024 | 5 |
| 2013-07-26.18 | 499.68 | 159.68 | – | 19.058 ± 0.053 | 17.814 ± 0.035 | – | – | 18.260 ± 0.032 | 17.073 ± 0.018 | 17.197 ± 0.029 | 5 |
| 2013-07-30.72 | 504.22 | 164.22 | – | 19.044 ± 0.038 | 17.753 ± 0.021 | – | – | – | – | – | 5 |
| 2013-07-31.43 | 504.93 | 164.93 | – | 19.090 ± 0.111 | 17.708 ± 0.044 | – | – | – | 17.096 ± 0.027 | 17.257 ± 0.046 | 3 |
| 2013-08-01.17 | 505.67 | 165.67 | – | 19.070 ± 0.150 | – | – | – | 18.384 ± 0.030 | – | – | 5 |
| 2013-08-04.12 | 508.62 | 168.62 | – | 19.039 ± 0.113 | 17.900 ± 0.044 | – | – | 18.350 ± 0.025 | 17.129 ± 0.017 | 17.285 ± 0.025 | 5 |
| 2013-08-06.18 | 510.68 | 170.68 | – | 19.047 ± 0.068 | 17.886 ± 0.031 | – | – | 18.392 ± 0.024 | 17.247 ± 0.037 | 17.413 ± 0.035 | 5 |
| 2013-08-11.97 | 516.47 | 176.47 | – | 19.073 ± 0.125 | 18.005 ± 0.049 | – | – | – | 17.186 ± 0.022 | 17.385 ± 0.036 | 5 |
| 2013-08-14.01 | 518.51 | 178.51 | – | 19.074 ± 0.080 | 18.035 ± 0.036 | – | – | 18.487 ± 0.028 | 17.231 ± 0.017 | 17.422 ± 0.035 | 5 |
| 2013-08-16.99 | 521.49 | 181.49 | – | – | 18.099 ± 0.051 | – | – | 18.563 ± 0.036 | – | 17.428 ± 0.035 | 5 |
| 2013-08-20.15 | 524.65 | 184.65 | – | – | – | – | – | 18.613 ± 0.125 | 17.227 ± 0.041 | 17.433 ± 0.072 | 5 |
| 2013-08-20.42 | 524.92 | 184.92 | – | 19.089 ± 0.122 | 18.078 ± 0.051 | – | – | – | – | – | 5 |
| 2013-08-24.38 | 528.88 | 188.88 | – | – | 18.002 ± 0.060 | – | – | – | – | – | 3 |
| 2013-08-25.36 | 529.86 | 189.86 | – | – | – | – | – | – | 17.267 ± 0.036 | 17.526 ± 0.071 | 3 |

**Table A2** – *continued*

| UT Date (yyyy/mm/dd) | JD 245 6000+ | Phase[a] (d) | *uvw*1 (mag) | *uvw*2 (mag) | *uvm*2 (mag) | *uvu* (mag) | *uvb* (mag) | *uvv* (mag) | Tel[b]/ Inst |
|---|---|---|---|---|---|---|---|---|---|
| *Swift* UVOT photometry | | | | | | | | | |
| 2013-02-21.18 | 344.68 | 4.68 | 13.404 ± 0.038 | 13.434 ± 0.042 | 13.301 ± 0.036 | – | – | – | 4 |
| 2013-02-21.94 | 345.44 | 5.44 | 13.486 ± 0.039 | 13.589 ± 0.052 | 13.442 ± 0.047 | 13.670 ± 0.052 | 15.010 ± 0.049 | 15.094 ± 0.056 | 4 |
| 2013-02-22.08 | 345.58 | 5.58 | 13.489 ± 0.037 | 13.629 ± 0.044 | – | – | – | – | 4 |
| 2013-02-22.51 | 346.01 | 6.01 | 13.616 ± 0.056 | 13.747 ± 0.071 | – | – | – | – | 4 |
| 2013-02-24.04 | 347.54 | 7.54 | 13.734 ± 0.035 | 14.133 ± 0.041 | 13.830 ± 0.035 | – | – | – | 4 |
| 2013-02-24.90 | 348.40 | 8.40 | 13.848 ± 0.043 | 14.363 ± 0.052 | 14.007 ± 0.037 | 13.819 ± 0.050 | 15.010 ± 0.046 | 14.962 ± 0.047 | 4 |
| 2013-02-24.98 | 348.48 | 8.48 | – | – | 14.083 ± 0.059 | – | – | – | 4 |
| 2013-02-27.30 | 350.80 | 10.80 | – | 14.895 ± 0.072 | – | – | – | – | 4 |
| 2013-02-27.98 | 351.48 | 11.48 | 14.395 ± 0.058 | 14.992 ± 0.072 | 14.742 ± 0.060 | 13.997 ± 0.051 | 15.072 ± 0.047 | 15.018 ± 0.049 | 4 |
| 2013-03-03.09 | 354.59 | 14.59 | 15.084 ± 0.060 | 15.792 ± 0.075 | 15.662 ± 0.063 | 14.340 ± 0.052 | 15.237 ± 0.047 | 15.132 ± 0.050 | 4 |
| 2013-03-06.13 | 357.63 | 17.63 | 15.635 ± 0.063 | 16.577 ± 0.082 | 16.574 ± 0.072 | 14.608 ± 0.052 | 15.258 ± 0.047 | 15.165 ± 0.049 | 4 |
| 2013-03-14.17 | 365.67 | 25.67 | 17.408 ± 0.116 | 18.759 ± 0.261 | 18.859 ± 0.320 | 15.680 ± 0.068 | 15.552 ± 0.054 | 15.220 ± 0.061 | 4 |
| 2013-03-18.21 | 369.71 | 29.71 | 17.710 ± 0.127 | 19.461 ± 0.364 | 19.231 ± 0.335 | 16.203 ± 0.066 | 15.739 ± 0.049 | 15.303 ± 0.051 | 4 |
| 2013-03-20.97 | 372.47 | 32.47 | 18.073 ± 0.153 | 19.120 ± 0.264 | 19.430 ± 0.385 | 16.458 ± 0.068 | 15.896 ± 0.049 | 15.354 ± 0.049 | 4 |
| 2013-03-27.97 | 379.47 | 39.47 | 18.913 ± 0.299 | 19.516 ± 0.549 | – | 17.096 ± 0.095 | 16.161 ± 0.054 | – | 4 |
| 2013-04-01.39 | 383.89 | 43.89 | 18.754 ± 0.266 | 19.548 ± 0.390 | 19.785 ± 0.538 | 17.276 ± 0.101 | 16.195 ± 0.053 | 15.439 ± 0.053 | 4 |
| 2013-04-05.20 | 387.70 | 47.70 | 18.935 ± 0.294 | 21.232 ± 1.634 | 19.854 ± 0.556 | 17.431 ± 0.105 | 16.391 ± 0.054 | 15.565 ± 0.053 | 4 |
| 2013-04-10.84 | 393.34 | 53.34 | 19.158 ± 0.359 | 20.750 ± 1.075 | 20.042 ± 0.671 | 17.637 ± 0.120 | 16.472 ± 0.055 | 15.548 ± 0.053 | 4 |
| 2013-04-21.92 | 404.42 | 64.42 | 19.450 ± 0.628 | – | – | – | – | – | 4 |
| 2013-04-26.01 | 408.51 | 68.51 | 19.505 ± 0.487 | – | 20.392 ± 1.262 | 17.890 ± 0.167 | 16.646 ± 0.087 | 15.615 ± 0.086 | 4 |
| 2013-05-01.32 | 413.82 | 73.82 | 20.646 ± 1.300 | 20.560 ± 0.882 | 20.642 ± 1.126 | 18.092 ± 0.160 | 16.728 ± 0.058 | 15.632 ± 0.054 | 4 |
| 2013-05-14.26 | 426.76 | 86.76 | 21.116 ± 2.278 | 20.650 ± 1.277 | – | 18.971 ± 0.456 | 16.825 ± 0.080 | 15.821 ± 0.080 | 4 |
| 2013-05-16.00 | 429.50 | 89.50 | – | – | 20.689 ± 1.217 | 18.496 ± 0.233 | 16.925 ± 0.066 | 15.858 ± 0.062 | 4 |
| 2013-05-20.95 | 433.45 | 93.45 | 20.929 ± 1.738 | 21.652 ± 2.536 | 20.850 ± 1.421 | 18.708 ± 0.279 | 17.223 ± 0.074 | 16.050 ± 0.067 | 4 |
| 2013-05-30.95 | 443.45 | 103.45 | 20.721 ± 1.389 | 21.184 ± 1.547 | 21.605 ± 2.708 | 19.429 ± 0.464 | 18.155 ± 0.115 | 16.923 ± 0.096 | 4 |

*Notes.* [a]with reference to the explosion epoch JD 245 6340.0[b]1: 104-cm Sampurnanand Telescope (ST) and 130-cm Devasthal fast optical telescope (DFOT), ARIES, India; 2: Faulkes Telescope South; 3: Faulkes Telescope North; 4: Swift UVOT data; 5: 1-m class telescopes of Las Cumbres Observatory Global Telescope (LCOGT) network; 6: IAU circular report.

**Table B1.** Journal of spectroscopic observations of SN 2013ab. The spectral observations are made at 25 phases from 2 to 184 d.

| UT Date (yyyy-mm-dd.dd) | JD 245 6000+ | Phase[a] (d) | Telescope[c] | Range[b] (μm) | Exposure (s) |
|---|---|---|---|---|---|
| 2013-02-18.70 | 342.20 | 2.20 | FTS | 0.32–1.00 | 1500 |
| 2013-02-19.74 | 343.24 | 3.24 | FTS | 0.32–1.00 | 1500 |
| 2013-02-24.71 | 348.21 | 8.21 | FTS | 0.32–1.00 | 1500 |
| 2013-02-28.59 | 352.09 | 12.09 | FTN | 0.32–1.00 | 1800 |
| 2013-03-01.08 | 352.58 | 12.58 | PEN | 0.00–0.00 | 1800 |
| 2013-03-01.50 | 353.00 | 13.00 | FTN | 0.32–1.00 | 1800 |
| 2013-03-02.51 | 354.01 | 14.01 | FTN | 0.32–1.00 | 1800 |
| 2013-03-03.51 | 355.01 | 15.01 | FTN | 0.32–1.00 | 1800 |
| 2013-03-04.59 | 356.09 | 16.09 | FTN | 0.32–1.00 | 1800 |
| 2013-03-06.71 | 358.21 | 18.21 | FTS | 0.32–1.00 | 2000 |
| 2013-03-17.93 | 369.43 | 29.43 | HCT | 0.38–0.84 | 1800 |
| 2013-03-19.63 | 371.13 | 31.13 | FTS | 0.32–1.00 | 2000 |
| 2013-03-31.58 | 383.08 | 43.08 | FTS | 0.32–1.00 | 2400 |
| 2013-05-01.84 | 414.34 | 74.34 | HCT | 0.38–0.84 | 1200 |
| 2013-05-03.35 | 415.85 | 75.85 | FTN | 0.32–1.00 | 3600 |
| 2013-05-04.33 | 416.83 | 76.83 | FTN | 0.32–1.00 | 3600 |
| 2013-05-04.85 | 417.35 | 77.35 | HCT | 0.38–0.68 | 1800 |
| 2013-05-05.08 | 417.58 | 77.58 | PEN | 0.00–0.00 | 1200 |
| 2013-05-09.57 | 422.07 | 82.07 | FTN | 0.32–1.00 | 3600 |
| 2013-05-15.85 | 428.35 | 88.35 | HCT | 0.38–0.84 | 1200 |
| 2013-06-14.64 | 458.14 | 118.14 | HCT | 0.38–0.68 | 2400 |
| 2013-07-13.34 | 486.84 | 146.84 | FTN | 0.32–1.00 | 3600 |
| 2013-08-09.25 | 513.75 | 173.75 | FTN | 0.32–1.00 | 3600 |
| 2013-08-18.25 | 522.75 | 182.75 | FTN | 0.32–1.00 | 3600 |
| 2013-08-19.25 | 523.75 | 183.75 | FTN | 0.32–1.00 | 3600 |

*Notes.* [a]With reference to the explosion time JD 245 6340.0.
[b]For transmission $\geq$50 per cent.
[c]HCT: HFOSC on 2-m Himalayan Chandra Telescope, India; FTN : FLOYDS on 2 m Faulkes Telescope North, Hawaii; FTS: FLOYDS on 2-m Faulkes Telescope South, Australia; PEN: B&C spectrograph on 1.22 m Galileo Telescope, Italy.

photometry, individual spectrum was multiplied by wavelength-dependent polynomial function and its *BVRI* filter-response convolved fluxes were compared with photometric fluxes at corresponding epoch. The multiplied polynomial was tuned to minimize the flux difference and obtain the tied spectrum. The one-dimensional spectra were corrected for heliocentric velocity of the host galaxy (1374 km $s^{-1}$; see Section 1) using *dopcor* tasks.

This paper has been typeset from a TEX/LATEX file prepared by the author.